

ISOCAM observations in the Lockman Hole - II

The 14.3 μm deep survey: data reduction, catalogue and source counts^{***}

G. Rodighiero¹, C. Lari², D. Fadda³, A. Franceschini¹, D. Elbaz⁴, and C. Cesarsky⁵

¹ Dipartimento di Astronomia, Università di Padova, Vicolo dell'Osservatorio 5, I-35122 Padova, Italy e-mail: rodighiero@pd.astro.it

² Istituto di Radioastronomia del CNR (IRA), via Gobetti 101, I-40129 Bologna, Italy

³ Spitzer Science Center, California Institute of Technology, Mail Code 220-6, Pasadena, CA 91126, USA

⁴ CEA, DSM, DAPNIA, Service d'Astrophysique, F-91191 Gif-sur-Yvette Cedex, France

⁵ European Southern Observatory (ESO), Karl-Schwarzschild-Strasse, 2, 85748 Garching bei München, Germany

Received date; accepted date

Abstract. We present a new analysis of the ISOCAM 14.3 μm deep survey in a 20×20 square arcmins area in the Lockman Hole. This survey is intermediate between the ultra-deep surveys and the shallow surveys in the ELAIS fields. The data have been analyzed with the method presented by Lari et al. (2001). We have produced a catalogue of 283 sources detected above the $5\text{-}\sigma$ threshold, with fluxes in the interval 0.1-8 mJy. The catalogue is 90% complete at 1 mJy. The positional accuracy, estimated from the cross-correlation of infrared and optical sources, is around 1.5 arcsec. The search for the optical counterparts of the sources in the survey is performed on a medium-deep r' band optical image (5σ depth of $r'=25$), making use of the radio detections when available. The photometry has been checked through simulations and by comparing the data with those presented in a shallower and more extended ISOCAM survey in the Lockman Hole, that we have presented in a companion paper. Only 15% of the 14.3 μm sources do not have an optical counterpart down to $r'=25$ mag. We use the 6.7/14.3 μm colour as a star/galaxy separator, together with a visual inspection of the optical image and an analysis of the observed Spectral Energy Distribution of the ISOCAM sources. The stars in the sample turn out to be only 6% of the sample. We discuss the 14.3 μm counts of extragalactic sources, combining our catalogue with that obtained from the shallower ISOCAM survey. The data in the two surveys are consistent, and our results fully support the claims in previous works for the existence of an evolving population of infrared galaxies, confirming the evident departure from non-evolutionary model predictions.

Key words. Infrared: galaxies – Galaxies: photometry, statistics, evolution – Cosmology: observations – Methods: data analysis

1. Introduction

The recent space missions (COBE, IRAS and ISO) devoted to the study of the Universe at long wavelengths have demonstrated that the infrared (IR) and sub-millimeter emission from galaxies is a main component of the energy budget of the extra-galactic background

Send offprint requests to: G. Rodighiero

* Based on observations obtained with the *Infrared Space Observatory*, an ESA science mission with instruments and contributions funded by ESA Member States and the USA (NASA).

** Tables 2 and 3 are available in electronic form at the CDS via anonymous ftp to [cdsarc.u-strasbg.fr](ftp://cdsarc.u-strasbg.fr) (130.79.128.5) or via <http://cdsweb.u-strasbg.fr/cgi-bin/qcat?J/A+A/>. Table 1 and Figures 1, 2, 9, 10, 11 will only be published in the electronic version of the Journal.

(Hauser & Dwek 2001). Actually, the cosmic infrared background (CIRB) includes an energy density comparable to that in the UV/optical background (Lagache et al., 1999; Bernstein et al. 2002) and is interpreted as the integrated emission by dust present in distant galaxies. The principal processes generating the IR emission are star formation and AGN activities. The relative contribution of the two is one of the key elements for the evolutionary models proposed up to now (i.e. Rowan-Robinson et al. 2001, Franceschini et al. 2001, Chary & Elbaz 2001, Xu et al. 2003). IR galaxy counts based on the IRAS data (Rowan-Robinson et al., 1984; Soifer et al., 1984) showed a marginally significant excess of faint sources with respect to “no-evolution” models (Hacking et al., 1987; Franceschini et al. 1988; Lonsdale et al., 1990; Gregorich et al., 1995; Bertin et al, 1997), but did not provide enough statistics and dynamic range in flux to discrim-

inate between evolutionary scenarios. More recently, the improved resolution and sensitivities of the Infrared Space Observatory (ISO, Kessler et al. 1996) detectors have provided deeper data that have been used to constrain the model predictions (such as source counts, redshift distributions and colours). The studies conducted on the mid-IR population have shown that these sources show remarkable properties compared with optically selected galaxy populations. The ISOCAM (Cesarsky et al. 1996) 14.3 μm source counts obtained by different surveys, over a wide flux range, indicate evidence of strong evolution at flux densities fainter than ~ 2 mJy (i.e. Elbaz et al. 1999; Flores et al. 1999; Lari et al. 2001; Metcalfe et al. 2001). Some evidence of evolution has also been detected by ISO at longer wavelengths (e.g. at 175 μm – Efstathiou et al. 2000, Dole et al. 2001, at 95 μm – Rodighiero et al. 2003, Rodighiero & Franceschini 2004).

In order to understand the nature of the mid-IR sources, Franceschini et al. (2003) and Elbaz et al. (2002) have matched the statistical and IR-spectral properties of the faint ISO sources detected at $\lambda_{eff} = 14.3\mu\text{m}$ with the spectral intensity of the CIRB and argue that, due to their high luminosity and moderate redshifts ($z \simeq 0.5$ to 1.3), these mid-IR sources represent the main contributors to the CIRB. Some evidence (Elbaz et al. 2004) suggests that most of the stars in today’s galaxies were formed during an active infrared phase, enhanced by the local environment. The CIRB is interpreted as a “fossil record” of these luminous infrared events (Elbaz & Cesarsky 2003), and it reflects the influence of the star formation induced by the interaction among galaxies. The same conclusion is reached by Franceschini et al. (2003), who compared the on-going star formation activity with the already formed stellar masses to estimate the time scales t_{sf} for the stellar build-up. From a morphological point of view, the faint ISOCAM galaxies appear to form a composite population, including moderately active but very massive spiral-like galaxies, and very luminous ongoing starburst irregular galaxies, in a continuous sequence. From the observed t_{sf} and assuming typical starburst time scales, Franceschini et al. (2003) infer that only a fraction of the galactic stars can be formed in each single starburst event, while several of such episodes during a protracted SF history are required for the whole galactic build-up.

The mentioned scenario is supported by the results of optical identifications of the faint sources detected in the deep ISOCAM surveys. Indeed, most of these sources are identified with relatively bright optical counterparts with a median redshift of $z \sim 0.7$. They are mainly dusty starbursts with large star formation often triggered by interactions ($\sim 30\%$ of them show optical signatures of interactions, Flores et al. 1999).

To explore these subjects, ISO has deeply surveyed sky regions where the HI absorption is very low. The Lockman Hole (Lockman et al. 1986), in particular, was selected for its high ecliptic latitude ($|\beta| > 50$) to keep the Zodiacal dust emission at a minimum, and for the low cirrus emission. This region presents the lowest HI column density

in the sky, hence is suited for the detection of faint IR sources. The data that we have analysed in the present work are a combination of a deep survey of 20×20 square arcminutes within the Lockman Hole region, and a shallower ISOCAM survey of 40×40 square arcminutes centred in the same position and completely overlapping the deeper one. The results on the complete Shallow region are presented in a separate paper (Fadda et al. 2004, hereafter Paper I). Here we consider only the data in the smaller and deeper combined area. The deep and shallow surveys of the Lockman Hole were performed as part of the ISOCAM guaranteed time extragalactic surveys (IGTES). Together with deeper surveys from the IGTES, they were used to build the number counts published in Elbaz et al. (1999). In this paper, we present the new 14.3 μm catalogue, obtained by analyzing the ISOCAM data with the technique described by Lari et al. (2001).

With this deep data-set we will span the flux range ($\sim 0.5 - 1$ mJy) where the slope of the ISOCAM source counts changes and strongly deviates from the Euclidean regime. The properties of our sample will then provide strong constraints on the evolution models for the IR galaxy populations.

The Spitzer Space Observatory (Werner et al., 2004) has recently observed the same region in the Lockman Hole in complementary spectral channels at 24, 70 and 160 μm with MIPS and in the near-IR with IRAC. This will provide additional extensive information on the Spectral Energy Distributions (SEDs) of ISO sources, complementary to the ISOCAM 14.3 μm information, given that the nearest Spitzer bands are centred at 8 and 24 μm .

The paper is organized as follows. Section 2 gives a summary of the ISOCAM observations. Section 3 describes the method used and summarizes the steps of the reduction, the map projection and the source extraction. The photometry is presented in Section 4, and the absolute calibration is presented in section 5. In Section 6 the mid-IR colours are discussed and Section 7 describes the optical identifications of the infrared sources, together with the position accuracy. The full catalogue is finally presented in Section 8 and the extra-galactic counts at the bright flux levels are discussed in Section 9. A summary of the work is then reported in Section 10.

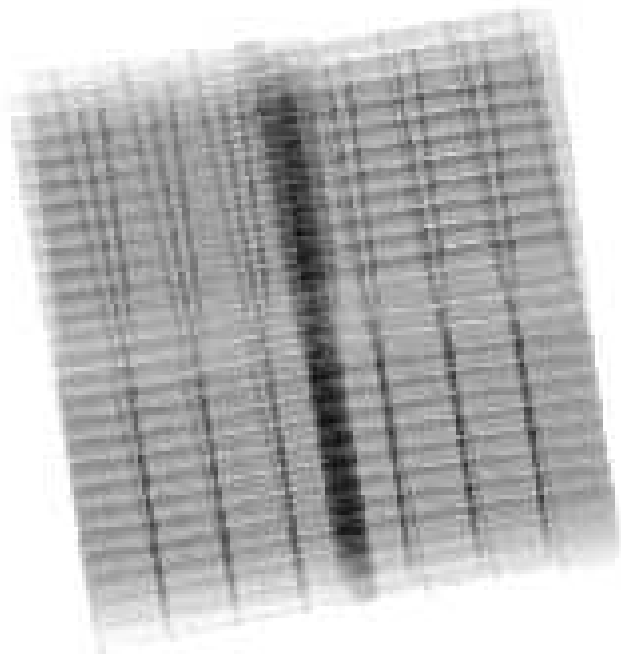
Forthcoming papers will discuss the redshift distribution of the sources using spectroscopic and photometric redshifts, the cross-correlation with the radio data and the relationship between star-formation and the mid-IR flux.

2. Observations

The Lockman Hole, an area with the lowest HI column density and cirrus emission ($< 0.4\text{MJy/sr}$, Lockman et al. 1986), has been observed by ISOCAM (on board the ISO satellite) at 6.7 and 14.3 μm over an area of 20×20 square arcminutes centred at 10:52:07 +57:21:02 (J2000), corresponding to the centre of the ROSAT HRI image. The

Table 1. ISOCAM Deep Lockman Hole observation parameters.

Parameter	LW3
Band effective wavelength	14.3 μm
Band width	6 μm
Detector gain	2
Integration time	5 s
Pixel field of view	6"
Nr. of horizontal and vertical steps	11 \times 4
Step sizes	54", 168"
Nr. of raster maps	8
Total area covered	0.14 deg ²

**Fig. 1.** Lockman Deep 14.3 μm sky coverage. Black regions correspond to ~ 2000 seconds of exposure time, grey regions to ~ 700 seconds.

field was deeply observed for a total of 45 ks at 14.3 μm (LW3 filter) and 70 ks at 6.75 μm (LW2 filter). The LW3 observation was done in raster mode: the squared configuration is composed of four sub-quadrants each repeated twice, for a total of 8 independent rasters. The observation parameters are reported in Table 1. In addition, a shallower survey at the same central position was done at 14.3 μm on a region of 40×40 square arcminutes for a total exposure time of 55 ks (Paper I). In this paper we present our new analysis and data reduction of the data in the combined area. The sky coverage is presented in Figure 1. The same field has been observed with the ISOPHOT instrument, at 90 μm and 170 μm (Rodighiero et al. 2003, Kawara et al. 2004). These same sources will be observed by IRAC and MIPS in the Spitzer Guaranteed Time.

In order to study the ISOCAM sources, a deep Sloan r' band image was obtained with the Wide Field Camera

(WFC) of the Isaac Newton Telescope at La Palma, Spain, for a total of 4 hours of integration (Fadda et al., in preparation).

The images have been reduced using IRAF packages (see Paper I for details). The photometric zero-point has been evaluated using the standard stars in the night with the best transparency and every image has been scaled to an image taken during this night.

The mean seeing is ~ 1.3 arcsec, and the magnitude limit is around 25 mag (computed within a circular aperture of $1.35 \times \text{FWHM}$ at a $5\text{-}\sigma$ level).

We have run SExtractor (Bertin & Arnouts 1999) on this image to get the r' band magnitudes: we adopted a $3 \times \text{FWHM}$ aperture magnitude and the *mag_auto* (i.e. the Kron fluxes) of SExtractor for extended sources.

3. Data reduction

The ISOCAM data presented in this work have been reduced with the method discussed in Lari et al. (2001). This procedure has been recently successfully applied to other deep and shallow surveys (Gruppioni et al. 2002, Pozzi et al. 2003, Vaccari et al. 2004). The description of the data reduction has been described in the cited articles, and a general discussion of the strategy that we used for the Lockman observations is also reported in Paper I.

3.1. The reduction pipeline

Summarizing, the reduction of ISOCAM data requires a careful treatment of various external and instrumental effects, in particular cosmic ray impacts (*glitches*) and detector hysteresis (i.e. the slow response of the detector to flux variations). To deal with all of them, the method discussed by Lari et al. (2001) was based on the assumption that the incoming flux of charged particles generates transient behaviours with two different time scales: a fast and a slow one.

The method basically consists of looking at the time history of each detector pixel and identifying the stabilisation background level. Then it models the glitches, the background and the sources with all the transients over the whole pixel time history.

The data are first corrected for short-time cosmic rays. The general background is then estimated as the stabilisation level along the whole time history of each pixel, and an initial guess of the fitting parameters is performed (see Vaccari et al. 2004). The signal as a function of time is finally processed, independently for each pixel. The fitting procedure models the transients along the time history, and the features on both short and long time scales produced by cosmic ray impacts. Furthermore, the code recognizes sources (above a given threshold level) and recovers all the time histories *reconstructing* the local background as it would appear in the absence of glitches.

The fitting algorithm starts with the brightest glitches identified in the pixel time history, assumes discontinuities at these positions, and tries to find a fit to the time history

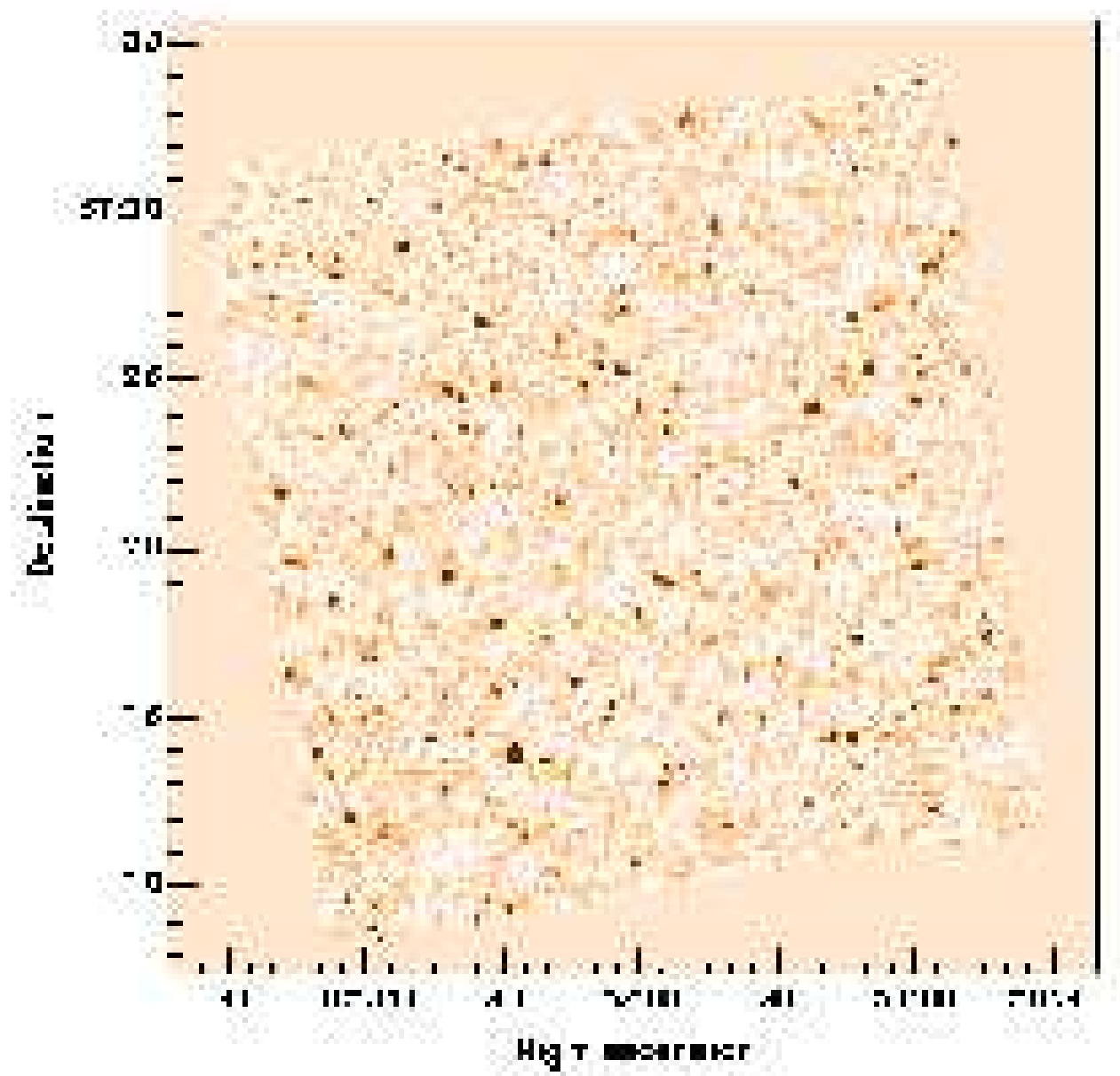


Fig. 2. Signal to noise map of the total field observed by ISOCAM in the direction of the Lockman Hole.

that satisfies the model assumed to describe the solid-state physics of the detector. By successive iterations, the parameters and the background for each pixel are adjusted to better fit the data, until the rms of the difference between model and real data is smaller than a given amount.

After the first run of the automatic fitting procedure, the next step is the interactive mending of fitting failures.

3.2. Map projection

Once a satisfying fit is obtained for all the pixels over the whole pixel history, the pipeline generates sky maps. An image for each raster position is created, by averaging the signals of all the readouts relative to that pointing

for each pixel. The signal is then converted to flux units (mJy pixel^{-1}), glitches and bad data are masked and the images are then combined to create the final raster maps (one for each raster position). These images are projected and combined onto a sky map (raster image) using the projection algorithm available for ISOCAM data in the CIA package (Cam Interactive Analysis, Ott et al., 2001). When projecting the signal on the sky, we apply to the nominal astrometry of each raster a median offset computed from the positions of those sources in common with the Lockman Shallow catalogue (see the astrometric calibration presented in Paper I).

The redundancy of Lockman ISOCAM observations allowed us to generate high resolution maps, rebinning

the original data into a final map with pixel size of 2×2 arcsec. The detector signal is distributed in a uniform way between the smaller pixels. This process allows a better determination of source positions. The signal to noise map of the $20' \times 20'$ field observed by ISOCAM in the direction of the Lockman Hole is shown in Figure 2.

3.3. Source extraction

As the adopted procedure (Lari et al. 2001) considers only the peak flux, we performed the source extraction using $6''$ pixels sampled at a distance of $2''$. Thus, the pixels of the image used for the extraction have a size $2'' \times 2''$ (see also Paper I). The source detection is performed on the signal-to-noise maps: our procedure selects pixels above a low flux threshold ($0.5 \mu\text{Jy pixel}^{-1}$) using the IDL Astronomy Users Library task called *find* (based on DAOPHOT's equivalent algorithm). Then we extract from the selected list only those objects with signal-to-noise ratio > 3 .

In the final stage of our reduction we perform simulations in order to re-project the sources detected on the raster map onto the pixel time history. In this way we are able to check the different temporal positions supposed to contribute to the total flux of each source. This procedure provides two main advantages: firstly, it allows us to recover the flux losses and obtain a cleaned measure of the total flux; secondly, the visual inspection of the temporal pixel histories improve the rejection of spurious detections (see Vaccari et al. 2004 for a more comprehensive description of Lari's procedures). We have simulated all sources detected with a signal-to-noise ratio > 3 .

To strengthen the reliability of the Lockman catalogue, we have combined our reduction procedure with the performances of the PRETI method (Starck et al. 1999, see also Elbaz et al 2004 in prep. for a comparison of PRETI and the technique by Lari et al., 2001). This tool is based on a wavelet analysis which allows the discrimination of mid-IR sources from cosmic ray impacts at the very limit of the instrument. It is called PRETI for Pattern REcognition Technique for ISOCAM data, because glitches with transient behaviours are isolated in the wavelet space, i.e. frequency space, where they present peculiar signatures in the form of patterns automatically identified and then reconstructed. We have run PRETI on the ISOCAM $14.3 \mu\text{m}$ data used in this paper and extracted an independent list of sources. We started our own reduction by checking these brightest PRETI detections with simulations along the pixel time histories. We then proceeded by checking all other fainter detections in our own source list. This approach stabilizes the completeness at bright flux levels, and it has been applied to ISOCAM ultra deep observations (Lari et al 2004, Elbaz et al 2004).

4. Photometry

The flux density S_ν at $14.3 \mu\text{m}$ of a source is computed by applying a correction factor to the measured peak flux f_s in order to have a measure of its "total" flux (Lari

et al., 2001). f_s is the value of the map in the position where the source is detected. It is computed from a cubic interpolation of the data (in units of $\mu\text{Jy/pixel}$, being the pixel of 6×6 arcsec rebinned in 3×3 subpixels).

The correction factor to obtain the total flux is computed by simulating a source (with a flux similar to that measured) in the detected position (see the autosimulation process in Lari et al 2001 and Vaccari et al. 2004). By applying this procedure to all the sources in our list, we can deduce the total flux for each entry in our catalogue. Since most of the sources are distant faint sources and the pixel field of view is quite large (six arcseconds), the method is applied to almost every source with a few exceptions. For extended sources aperture photometry is used.

A comparison of the use of f_s with respect to aperture photometry has been discussed by Lari et al. (2001) and Vaccari et al. (2004). The implications for the choice of using only the central brightest pixel instead of an aperture on the central position of the source, when computing the total fluxes, will also be discussed in a forthcoming paper (Elbaz et al., 2004).

Extensive simulations in wider samples (e.g. ELAIS, Gruppioni et al. 2002) have shown that various statistical effects (such as the fact that the actual position of an infrared source is poorly known or the projection process itself) prevent the accurate reconstruction of the total flux of a source. However, with simulations we can quantify this bias (called q_{med}) and statistically recover flux losses. In Paper I, we discuss the simulations performed in the Lockman Shallow ISOCAM survey: the derived value of q_{med} is 0.84. This means that the total flux computed after the autosimulation has to be incremented by 16%.

In our new analysis of the Lockman Deep observations, we choose to apply the same factor derived for the Shallow case. We have separately quantified the effects of overlapping rasters on the flux lost.

The Shallow map presented in Paper I is composed of four rasters with only small overlap. On the contrary, our Deep map is the combination of twelve independent rasters, divided in four quadrants, each made of three rasters completely overlapping (Section 2).

Performing the source extraction on the single rasters and on the combined map, we can estimate the flux for each source in the single and in the mosaic maps. In Figure 3 we compare the ratio between the $14.3 \mu\text{m}$ mean fluxes computed from the single rasters and that from the final combined mosaic, as a function of their signal-to-noise ratio on the mosaic. We take into account only sources detected in at least three rasters. This ratio is almost constant down to a signal-to-noise > 10.5 , the scatter at fainter values being mainly due to the noise that dominates the determination of fluxes in the single rasters.

As indicated by the plot, the fluxes extracted from the mosaic map tend to be statistically lower than that measured on the single maps. This can be due to small fluctuations on the astrometric offsets applied to the rasters, and to the projection itself: the mean effect is the broad-

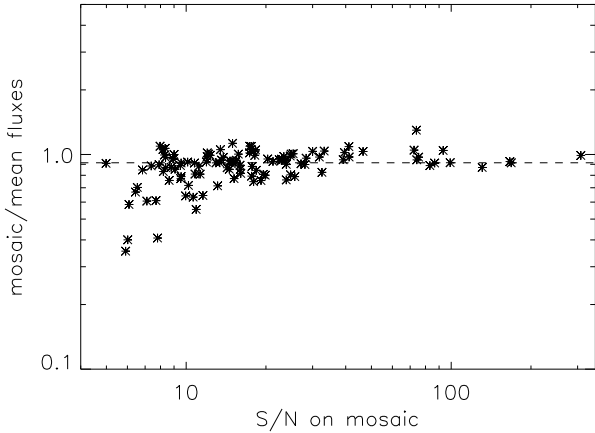


Fig. 3. 115 sources with three independent detections have been used to compute the photometric bias caused by the mosaicing of repeated rasters. The ratio between the $14.3 \mu\text{m}$ mean fluxes and the corresponding mosaic fluxes are plotted as a function of their signal to noise ratio on the mosaic. The horizontal line indicates the median ratio ($\text{bias_mos}=0.915$) that we will use to correct the total fluxes extracted from the mosaic.

ening of the source in the mosaic, with a corresponding lower peak flux.

Considering only those sources with three independent detections, we can constrain the mean correction factor for recovering the underestimated fluxes. This is done in Figure 3, where the horizontal line shows the median value of the ratio, that is $\text{bias_mos}=0.915$. We adopt this factor to further correct the total fluxes.

In the following, “measured fluxes” will refer to the total fluxes corrected for the flux bias (q_{med}) and the mosaicing bias (bias_mos).

5. Calibration of the LW3 deep catalogue

The corrections that we have applied to the $14.3 \mu\text{m}$ total fluxes (q_{med} and bias_mos) should have gives the fluxes of the sources in the Deep catalogue on the same scale as those in the Shallow catalogue. This is confirmed by directly comparing the total fluxes measured for the sources in common in the two samples. Figure 4 shows that for sources brighter than 0.25 mJy (crosses) the correlation follows the unitary relation (dashed line). Below 0.25 mJy in the Shallow survey only bright sources located over positive noise peaks are detected and there flux enhanced (see discussion in Paper I).

In Paper I we have checked that the LW3 fluxes of the Lockman Shallow (corrected for the flux bias $q_{med}=0.84$) are consistent with the predictions of stellar atmosphere models at $14.3 \mu\text{m}$, when considering the multi-wavelength photometry (optical, near- and mid-infrared) of the stars in the sample. Here, we compared the $14.3 \mu\text{m}$ total fluxes with the predictions by Aussel & Alexander (2001), who performed a detailed study of mid-infrared emission

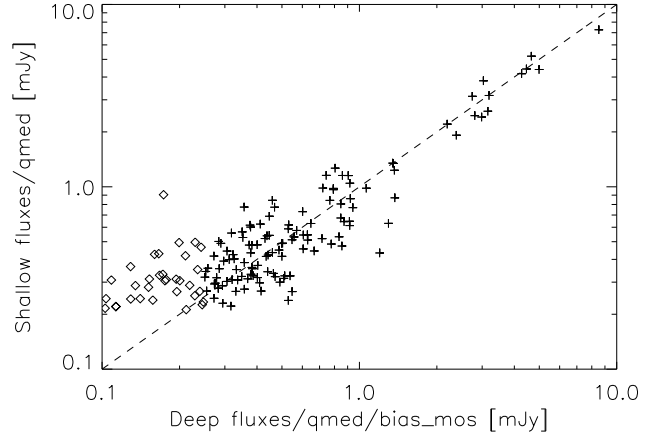


Fig. 4. Correlation of $14.3 \mu\text{m}$ total fluxes for the sources in common in the Shallow and in the Deep catalogues. Fluxes in the Deep have been corrected for the effect of the combination of repeated rasters ($\text{bias_mos}=0.915$) and for the same flux bias as in the Shallow catalogue ($q_{med}=0.84$). For sources above 0.25 mJy (crosses) the correlation follows the unitary relation (dashed line).

from stars. They exploited large samples from the IRAS Faint Source Catalog with counterparts in the 2MASS and Tycho-2 (Hog et al. 2000) catalogues. One of their findings is that the $J - K$ colour of stars is extremely well correlated with the $K - [12]$ colour, where [12] is a magnitude scale constructed from the IRAS $12 \mu\text{m}$ flux (Omont et al. 1999). This relation allows the accurate prediction of the $12 \mu\text{m}$ IRAS flux of a star, provided that its $J - K$ is known and within a certain limit. Stellar atmosphere models (Lejeune, Cuisinier & Buser 1998) indicate that the ratio of the $14.3 \mu\text{m}$ flux to the $12 \mu\text{m}$ flux of stars is constant, at least for spectral types hotter than K3. We have adopted this criterion to predict the $14.3 \mu\text{m}$ fluxes of the stars in the Lockman Shallow (see Paper I) and in the deeper area. The relations that we used in order to predict ISO $14.3 \mu\text{m}$ fluxes are:

$$K - [LW3] = 0.044 + 0.098(J - K), \quad (1)$$

where $[LW3]$ is a magnitude scale defined as

$$[LW3] = 3.202 - 2.5 \log(S_{LW3}[\text{mJy}]). \quad (2)$$

We have obtained the J and K magnitudes for 61 sources in our Deep sample from the deep 2MASS Survey of the Lockman Hole (Beichman et al. 2003). Using the previous equations, we have computed the predicted $14.3 \mu\text{m}$ flux for these sources and compared it with the measured one. The result is presented in Figure 5: the $14.3 \mu\text{m}$ measured fluxes are compared with the corresponding ratio of the measured over the predicted fluxes. As expected, the ratio is close to 1 for stars (asterisks), and greater for galaxies (diamonds). The intermediate objects (squares) should correspond to elliptical galaxies. We have verified

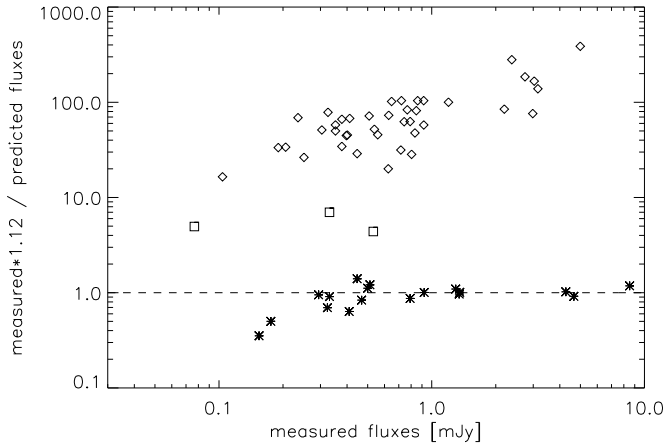


Fig. 5. The LW3 measured fluxes are compared with the corresponding ratio of the measured over predicted fluxes. This makes sense for sources with reliable K and J magnitudes (see text for details). As expected, the ratio is close to 1 for stars (asterisks), and greater for galaxies (diamonds). The intermediate objects (squares) should correspond to elliptical galaxies.

that the 18 sources with ratios close to 1 are all stars on the optical image. The median of this ratio for stars is 1.12, as found in Paper I for the stars in the Shallow sample. Given the poor statistics (18 objects), this value is consistent within $1\text{-}\sigma$ with that obtained on much wider samples for the ELAIS surveys: Gruppioni et al. (2002) and Vaccari et al. (2004) found a constant factor of 1.0974. This $\sim 10\%$ should be attributable to discrepancies between the independently established IRAS and ISO calibrations.

We decided to apply this factor to the fluxes when computing the galaxy counts (Section 9), in order to compare different samples on the same flux scale.

6. LW2/LW3 colour

As mentioned in Section 2, the Lockman Deep area has been observed both at 14.3 and at $6.7\ \mu\text{m}$. We have applied the reduction procedure described in Section 3 only to the longer wavelength ISOCAM data, however exploiting the PRETI pipeline we obtained a LW2- $6.7\ \mu\text{m}$ map and checked for the counterparts of the LW3- $14.3\ \mu\text{m}$ list (the same dataset has also been used in Fadda et al. 2002). Starting from the signal to noise map, we applied the same extraction tool as we did for the LW3 band (Section 3.3) and obtained a catalogue with the measure of the peak fluxes.

We computed the correction factor to derive the total fluxes using as a calibrator the relations by Aussel & Alexander (2002), as we did for the $14.3\ \mu\text{m}$ (Section 5). In this case the $6.7\ \mu\text{m}$ predicted fluxes were obtained through the following expressions:

$$K - [LW2] = 0.044 + 0.098(J - K), \quad (3)$$

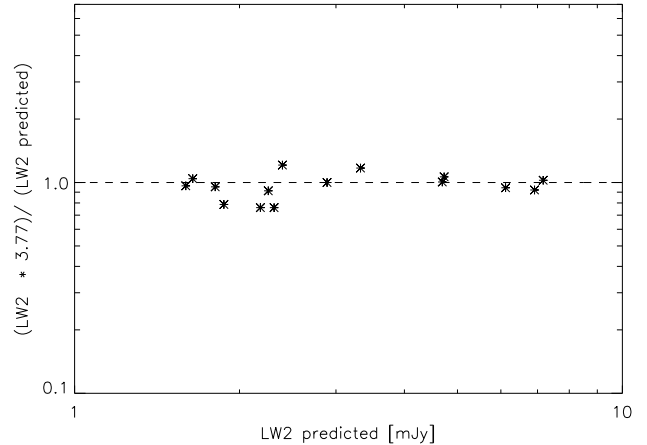


Fig. 6. We have calibrated the LW2- $6.7\ \mu\text{m}$ fluxes against model predictions (Aussel & Alexander 2002). The figure shows that for the stars with J and K counterparts, the $6.7\ \mu\text{m}$ total fluxes are derived by multiplying for a factor 3.77 the corresponding peak fluxes.

where $[LW2]$ is a magnitude scale defined as

$$[LW2] = 4.860 - 2.5\log(S_{LW2}[\text{mJy}]). \quad (4)$$

The 17 sources with J, K and $6.7\ \mu\text{m}$ detections and optical stellar shapes are used to calibrate the $6.7\ \mu\text{m}$ total fluxes: we found the correction factor to be 3.77 (see figure 6). We did not perform other analyses to derive a more accurate absolute calibration. In fact a relative scale is enough for our purpose, as we are mainly interested in using the $6.7/14.3\ \mu\text{m}$ colour as a star/galaxy separator.

By cross-correlating the LW2 and LW3 catalogues, we found 63 objects with both detections: their colour-magnitude diagram is plotted in Figure 7.

In the plot the regions occupied by stars (asterisks) and galaxies (open diamonds) are clearly separated, as expected given the different spectra of the two classes. The consistency of this approach is supported by the consideration that the 18 stars identified with the LW2/LW3 ratio are exactly the same found from the predictions of the $14.3\ \mu\text{m}$ fluxes (see Section 5 and Figure 5).

The identifications of stars in the sample is important, given that these objects must be neglected when computing galaxy counts (Section 9).

7. Optical identifications

One of the best ways to look at the properties of faint infrared sources and study their evolution is to check their optical morphologies. Although only deep space observations allow a comprehensive view of the fainter population, we have attempted to perform the optical identifications of the Lockman Deep sources. Given the good quality of the optical R image ($R_{\text{lim}}=25$ mag, Section 2) we are able to make reliable associations with the infrared sources and

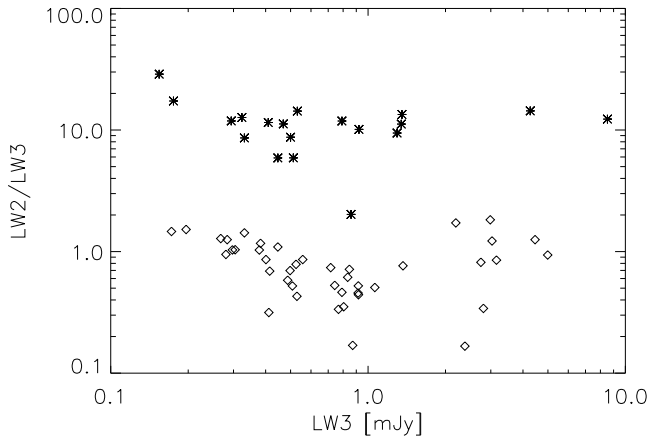


Fig. 7. For the 63 sources with both LW2 and LW3 detections, the $14.3 \mu\text{m}$ fluxes are plotted against the ratio of the 6.7 and $14.3 \mu\text{m}$ fluxes. As a first approximation, this ratio can be used as a star/galaxy indicator. Sources with high LW2/LW3 should correspond to stars (asterisks in the figure).

the corresponding optical counterparts. The mean separation between the optical and the infrared position is of the order of $1.5''$, the maximum separation being $\sim 4''$ (see discussion below).

We assume the r' band catalogue as our reference optical catalogue, which is used to search for the optical counterparts of the ISO sources using the likelihood ratio technique described by Sutherland & Saunders (1992). We adopt the procedure discussed in Pozzi et al. (2004): the likelihood ratio (LR) is the ratio between the probability that a given source at the observed position and with the measured magnitude is the true optical counterpart, and the probability that the same source is a chance background object. For each ISO source we adopted a mean positional error of 2 arcsec, and we assumed a value of 0.1 arcsec as the optical position uncertainty. We choose a search radius of 10 arcsec from the infrared position to look for the possible optical counterparts.

For each optical candidate the reliability (REL) is computed by taking into account, if needed, the presence of other optical candidates for the corresponding ISO source (Sutherland & Saunders 1992). Once the likelihood ratio has been calculated for all the optical candidates, one has to choose the best threshold value for LR (LR_{th}) to discriminate between spurious and real identifications. As the LR threshold we adopted $LR_{th} = 0.5$. With this value, all the optical counterparts of the ISOCAM sources with only one identification (the majority in our sample) and $LR > LR_{th}$ have a reliability greater than 0.8 (we assumed a value of $Q=0.9$ for the probability that an optical counterpart of the ISOCAM source is brighter than the magnitude limit of the optical catalogue, see Ciliegi et al. 2003, for more details). Using a less conservative value

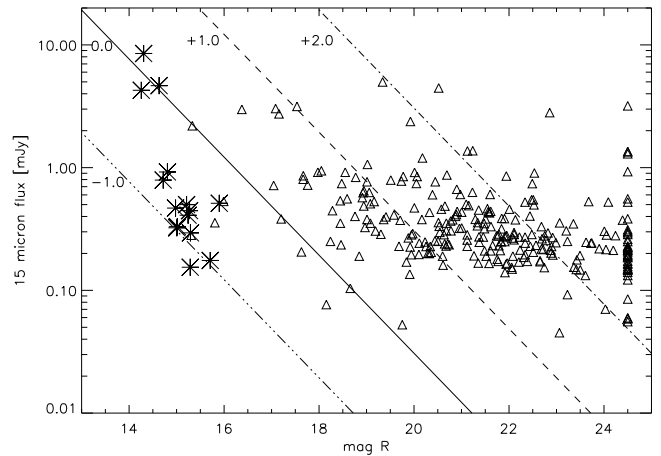


Fig. 8. LW3 fluxes as a function of the optical r' magnitudes for the Lockman Deep ISOCAM sources. The lines indicate the relations where the infrared to optical ratio is constant ($S(15\mu\text{m})/S_R = -1, 0, +1, +2$). The brightest objects are stars (marked as asterisks): the two exceptions correspond to stars blended with galaxies.

of $LR_{th}=0.2$ we found the same number of ISO/optical associations.

Moreover, we have checked by visual inspection the optical associations of each infrared source. With stars and isolated objects the cross-correlation is unambiguous: the shape and the peak of the infrared contours overlaid on the R image have confirmed the associations. However, in the case of extended ISO sources, where the confusion starts to play a role, the correlation between infrared and optical catalogues is much more uncertain: there are no unique associations. Several optical sources could lie inside the ISO detection and contribute to the infrared emission. When more than one optical candidate with $LR_{th} > 0.5$ is present for the same ISO source, we assume that the object with the highest likelihood ratio value is the real counterpart of the ISO source. However, when a radio emission is detected (~ 30 cases), the tight correlation with the infrared emission allows us to associate the ISO positions with the radio ones.

With this threshold value, 85% of the ISO sources have a likely identification. A percentage of 15% of the $14.3 \mu\text{m}$ sources do not present any optical reliable identifications down to the optical limits ($r' \sim 25$ mag), and are marked as blank fields. As suggested by Gonzalez-Solares et al. (2004), blank fields are probably the extreme version of the objects with high infrared to optical ratios ($S(15\mu\text{m})/S_R > \sim 10^3$). This is shown in Figure 8), where we plot the LW3 $14.3 \mu\text{m}$ fluxes as a function of the optical r' magnitudes for the Lockman Deep ISOCAM sources. The lines indicate the relations where the infrared to optical ratio is constant ($S(15\mu\text{m})/S_R = -1, 0, +1, +2$). We do not find evidence for a connection between the r' magnitude and the $14.3 \mu\text{m}$ flux density.

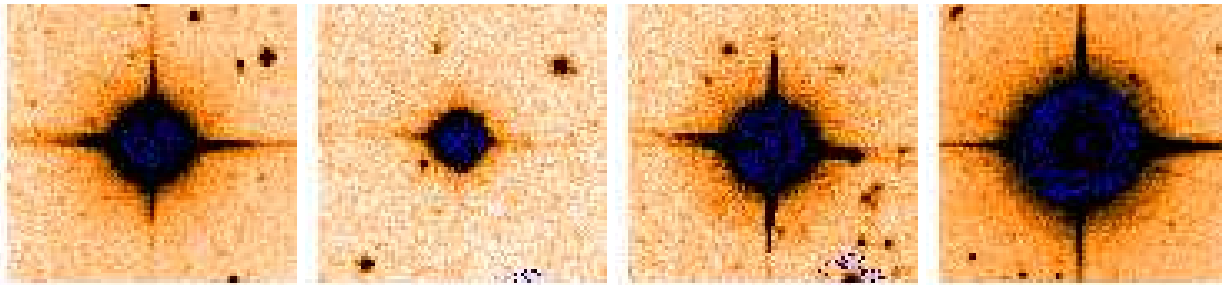


Fig. 9. Examples of few STARS in the $14.3 \mu\text{m}$ Lockman catalogue. We report the postage stamps of the R optical image overlaid with the $14.3 \mu\text{m}$ contours (starting from $5\text{-}\sigma$ at increasing signal-to-noise levels). Each map is $\sim 1 \times 1$ square arcminutes. North is upward, East leftward.

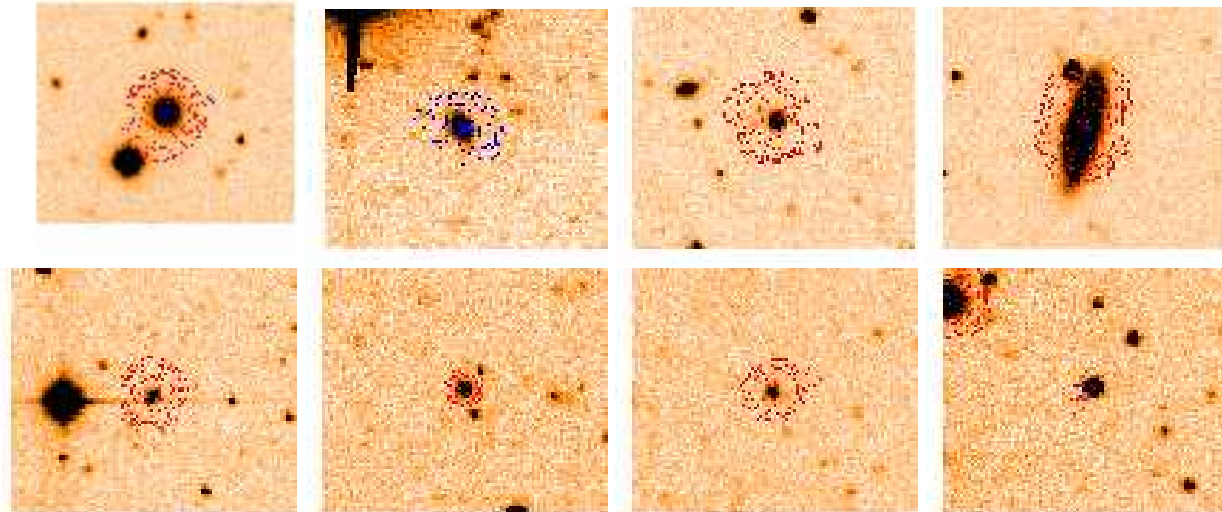


Fig. 10. Examples of few ISOLATED OBJECTS in the $14.3 \mu\text{m}$ Lockman catalogue. For this class of sources the optical identification is generally straightforward. The reference for the maps legend is the same as in Figure 9.

Apart from stars, we found that the infrared sources in our catalogue can be separated into two main classes: isolated objects, and blended objects. The second class is mainly composed of interacting galaxies (mergers) and small groups. In Figures 9-11 we present some examples for each of the mentioned morphological classes.

We used stars and isolated objects with unambiguous optical identifications to measure the astrometric uncertainties of the infrared sample. The results are plotted in Figure 12, where we have considered the distributions of the difference in right ascension and declination between the infrared and the optical positions (determined as discussed in Section 7). By fitting the histograms with a Gaussian function, the $3\text{-}\sigma$ limits of the distributions are, respectively, ~ 2.9 arcsec for the right ascension and ~ 3.7 arcsec for the declination. Of the 167 sources considered, $\sim 80\%$ lie within $[-1.5, +1.5]$ arcsec both in RA and DEC.

8. The catalogue

The final catalogue obtained with our method contains 283 sources detected at $14.3 \mu\text{m}$ in a $20' \times 20'$ region centred on the Lockman Hole. All sources have a signal-to-

noise ratio greater than 5. The entries are as detailed in the following:

- **Number** : source identification number;
- **Name** : IAU source name, referring to the name of the satellite (ISO) and to the identification of the survey (LHDS);
- **RA (J2000)** : Right Ascension at epoch J2000 in sexagesimal units;
- **DEC (J2000)** : Declination at epoch J2000 in sexagesimal units;
- **S/N** : signal to noise ratio;
- **Total Flux** : source total flux obtained from the peak flux or aperture photometry, expressed in mJy (the corresponding errors have been computed as discussed by Gruppioni et al 2002 and Vaccari et al. 2004, mainly taking into account the contribution of two effects, namely the autosimulation process and the noise present on the sky maps). An asterisk before the flux value indicates that for this source aperture photometry has been performed;
- **Radio Flux** : radio 1.4GHz flux density expressed in mJy (from De Ruiter et al. 1997 and Ciliegi et al. 2003);

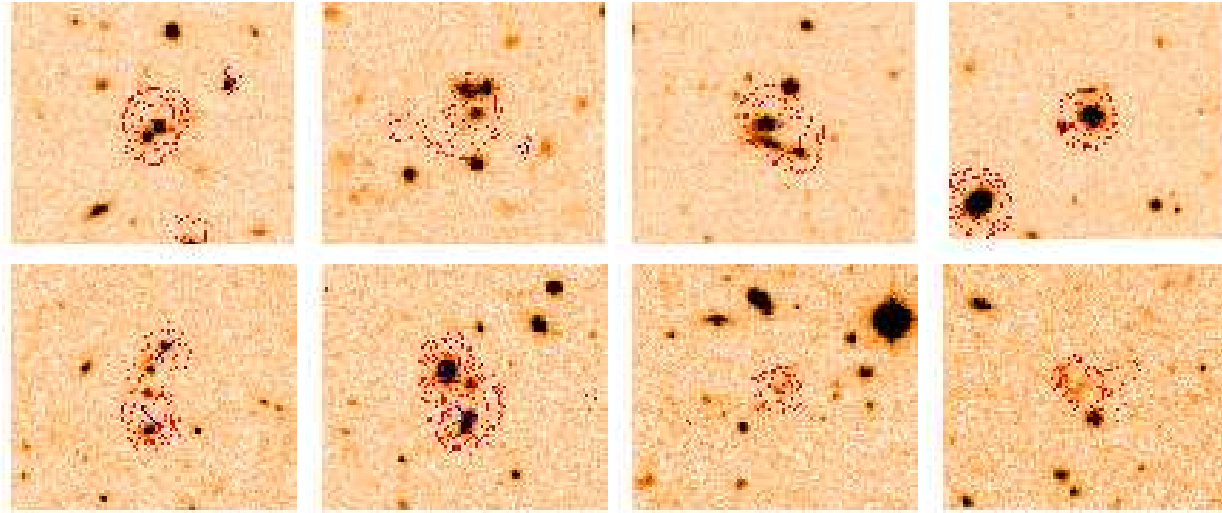


Fig. 11. Examples of a few BLENDED OBJECTS: as can be seen in the figure, they look like mergers or small groups. For these sources in the catalogue list we report the main optical associations within a search radius of 10 arcsec (from the major component to those with decreasing significance). The reference for the maps legend is the same as in Figure 9.

- **S/G** : flag for star (1) or galaxy (0);
- **REL** : reliability of the optical counterpart, when available;
- **r' magnitude** : optical r' Sloan magnitudes in the Vega system. For objects with multiple optical counterparts we assume that the object with the highest likelihood ratio value is the real counterpart of the ISO source. B.F. stands for Blank Field;
- $\Delta(IR - opt)$: distance in arcseconds between the infrared position and its optical association.

The complete catalogue is reported in Tables 2-3.

The flux distribution of the catalogue sources is illustrated in Figure 13 as a solid line, and is compared to the distribution of the Lockman Shallow catalogue (dotted line, see Paper I). 50% of the sources have fluxes greater than 0.3 mJy, $\sim 80\%$ greater than 0.19 mJy and $\sim 90\%$ greater than 0.16 mJy. As can be clearly seen from the two separately plotted histograms, sources in non-repeated regions (i.e. the Shallow sample) increase in number down to about 0.3 mJy, at which flux their number per flux bin drop sharply. Conversely, the number of sources per flux bin in repeated regions (i.e. the Deep sample) continues to increase down to 0.15 mJy. We note that the high reliability of the catalogue in the Shallow survey has been estimated to be above ~ 0.45 mJy (this level corresponds to the 20% completeness limit, see discussion in Paper I). Given that the ratio of the median exposure times (t_{exp}) of the Deep and of the Shallow maps is of the order of ~ 4 , and that the sensitivity is proportional to $\sqrt{t_{exp}}$, we assume a cutoff of ~ 0.22 mJy as a strong confidence level for the catalogue presented in this paper. Below this flux, a few spurious detections could contaminate the reliability of the source list. For this reason we have split the catalogue into two different tables: Table 2 lists the highly

reliable detections. In Table 3 we report the faint detections (flux < 0.22 mJy).

Images in fits format and catalogues in ASCII format are made publicly available through the world-wide-web¹ or directly on request from the authors.

9. Extragalactic source counts

In a forthcoming paper (Lari et al. 2004), we will discuss in detail the completeness and the source counts down to the fainter flux level reachable with the present and the Shallow samples (~ 0.2 mJy). This is to be done by performing intensive simulations at different flux levels and spatial scales. However, in this work we will attempt to characterize the statistical properties of our different 14.3 μm samples (Lockman Deep and Shallow) at the bright levels with the presently available data (catalogues and simulations in the shallower survey).

We have computed the 14.3 μm source counts down to a flux level of 0.5 mJy. We excluded the stars from the computation. The counts have been obtained by weighting each single source for the effective area corresponding to that source flux. In order to compare the two surveys, we plot in Figure 14 the respective sky coverages as a function of the peak flux (these are obtained by computing the sky area in the noise map with a signal lower than a given amount, spanning the range of the peak fluxes in the survey). It is evident that, above 0.1 mJy in peak flux units, the area weight does not affect the counts in both surveys. This converts to about 0.5 mJy in total flux units, meaning that above this flux level, in princi-

¹ via anonymous ftp to cdsarc.u-strasbg.fr (130.79.128.5) or via <http://cdsweb.u-strasbg.fr/cgi-bin/qcat?J/A+A/>, <http://spider.ipac.caltech.edu/staff/fadda/lockman.html> and <http://irsa.ipac.caltech.edu/data/SPITZER/SWIRE>

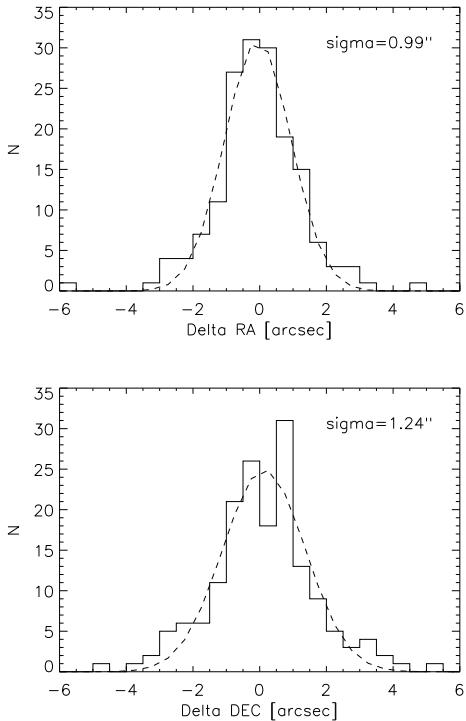


Fig. 12. Distribution of the difference in RA (*top*) and DEC (*bottom*) between the infrared coordinates and the positions of the optical identifications. In these graphics only sources with highly reliable optical counterparts (stars and isolated objects) have been considered. The distributions have been fitted with Gaussian functions, with dispersion of respectively 0.99'' and 1.24'' for RA and DEC.

ple, the Deep and the Shallow catalogues should have a similar incompleteness factor. We can verify this assumption by directly comparing the cumulative source counts in the two areas, without applying any correction. This is done in Figure 15: the integral counts are in perfect agreement above 0.5 mJy. Below this level, the shallower sample (dashed line) is more affected by incompleteness compared to the deeper one (solid line). Above ~ 0.9 mJy the Lockman Deep statistics are insufficient (see Figure 13) and the computed counts are meaningless. We then reasonably assume that, above 0.5 mJy, we can apply to both samples the incompleteness derived through simulations in Paper I for the Lockman Shallow. At 1 mJy almost all the sources are detected, and thus the samples are nearly complete ($\sim 90\%$) at this level. At 0.7 mJy we expect our sample to be $> 70\%$ complete (see Figure 7 in Paper I). This completeness level is very close to that found for the ELAIS S2 field (Pozzi et al. 2003).

To compare our results with those reported in the literature (Gruppioni et al, 2002, Lari et al. 2004), we multiplied the fluxes by the constant factor of 1.0974 (see discussion in Section 5) in order to compare different samples on the same flux scale (i.e. the IRAS scale). This factor

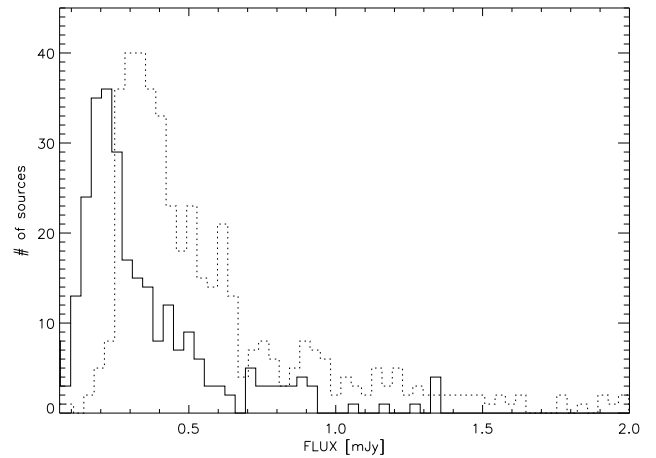


Fig. 13. Histogram Flux Distributions of the Lockman Deep sources (solid line) compared to that in the Lockman Shallow (dotted line).

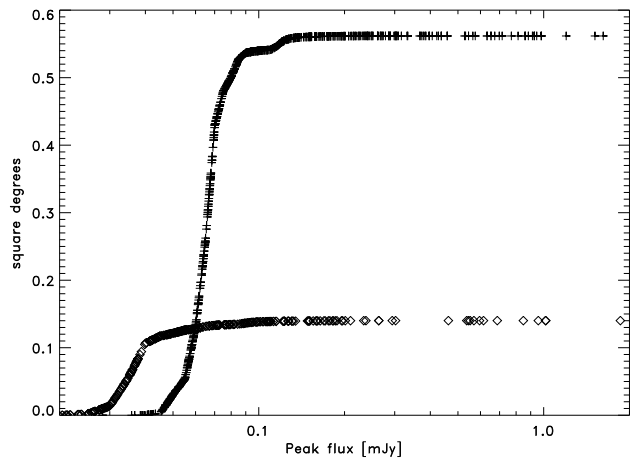


Fig. 14. Sky coverage as a function of the peak flux in the Lockman Deep and in the Lockman Shallow surveys. Above ~ 0.1 mJy the areal correction does not affect the two samples.

is correlated to discrepancies between the independently established IRAS and ISO calibrations.

The errors associated with the counts in each level have been computed as $\sqrt{\sum_i 1/A_{eff}^2(S_i)}$ (Gruppioni et al. 2002), where the sum is for all the sources with flux density S_i and $A_{eff}(S_i)$ is the effective area. The contributions of each source to both the counts and the associated errors are weighted for the area within which the source is detectable. The errors represent in any case the Poissonian term of the uncertainties, and have to be considered as lower limits to the total errors.

In Figure 16 we report the differential $14.3 \mu\text{m}$ counts normalized to the Euclidean law ($N \propto S^{-2.5}$). For the Lockman Deep survey, we have limited the computation to between 0.5 and 1 mJy. Below 0.5 mJy we need to improve the simulations to get a more reliable completeness

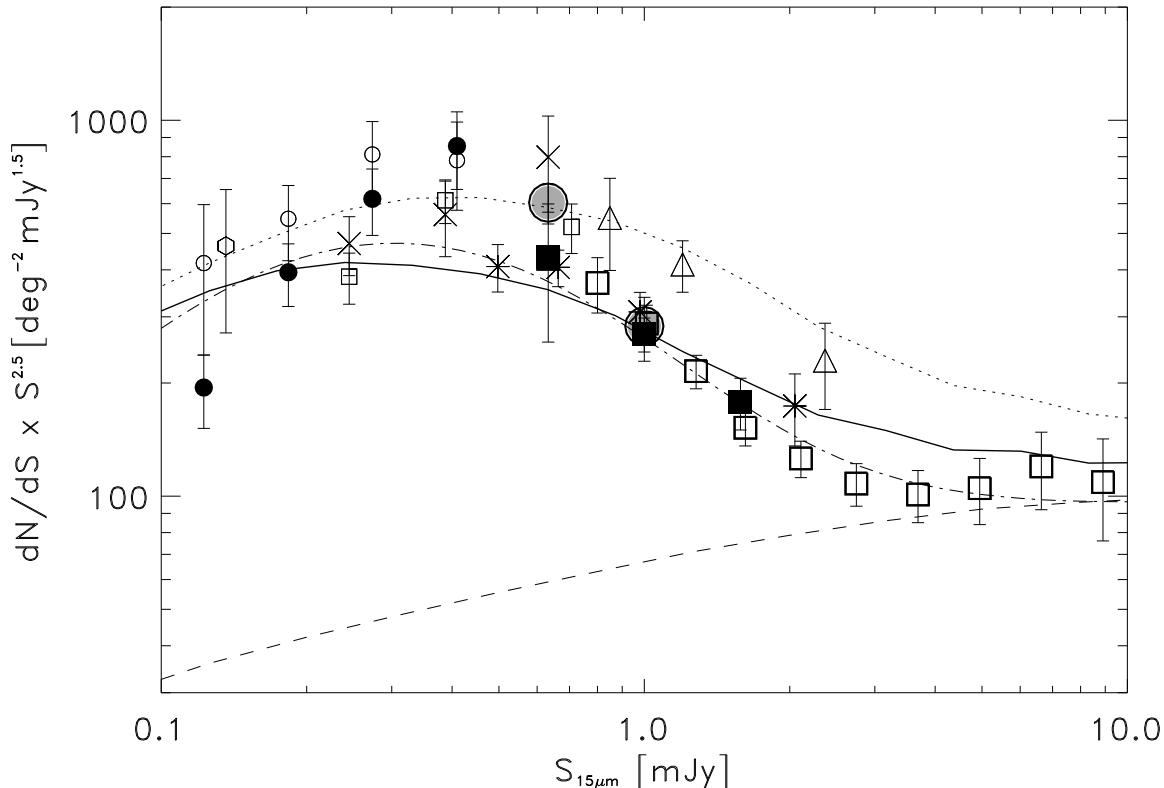


Fig. 16. $14.3 \mu\text{m}$ differential counts normalized to the Euclidean law ($N \propto S^{-2.5}$). Our estimates (Lockman Deep – grey filled circles, Lockman Shallow – black filled squares) are compared with those from other ISOCAM surveys (A2390 from Altieri, Metcalfe & Kneib (1999) – hexagon; ISO Hubble Deep Field North (HDF-N) from Aussel et al. (1999) – filled circles; ISO Hubble Deep Field South (HDF-S) – open circles, Marano Firback – thin open squares, Marano Ultra-Deep – crosses, Marano Deep – asterisks, and Lockman Deep – triangles from Elbaz et al. (1999); ELAIS S1 from Gruppioni et al. 2002 – thick empty squares). The data are compared with model predictions: Franceschini et al. (2001, dotted line), Franceschini et al. (2004 in prep., solid line), Pozzi et al. (2004, dot-dashed line). The dashed line represents the expectations from a no-evolution model normalized to the IRAS $12 \mu\text{m}$ local luminosity function (Fang et al. 1998).

estimate, above 1 mJy the number of bright sources drops (see Figure 13) and the statistics are insufficient.

The results presented in this work are in quite good agreement with those already published. However, the counts by Elbaz et al. (1999) in the Lockman Deep region (open triangles in Fig. 16) are systematically higher than ours. On the one hand, in our analysis we have accurately identified stars by means of the optical r' band image, and with an objective criterion based on the colour and on the SEDs of the LW3 sources (Sections 5 and 6). On the other hand, our procedure is different from that used by Elbaz et al. (1999). In any case, it has been carefully checked by using the stellar fluxes, thus providing high fidelity photometry. The good agreement with the results of Gruppioni et al. (2002) in the ELAIS fields, could suggest that a re-analysis of the other deep- and ultra-deep fields might slightly lower the corresponding ISOCAM counts over these flux ranges (this will be done in a separate paper by Lari et al. 2004).

When the data are compared with predictions, they turn out to be consistent with the expectations of a slightly modified version of the model by Franceschini et al. (2001). This multi-wavelength evolution model was designed to reproduce in particular the observed statistics of the ISOCAM mid-IR selected sources, but it also accounts for data at other IR and sub-millimetric wavelengths. The model assumes the existence of three basic populations of cosmic sources characterized by different physical and evolutionary properties: a population of non-evolving quiescent spirals, a population of fast evolving sources (including starburst galaxies and type-II AGNs) and a third component considered - but always statistically negligible - are type-I AGNs. The fraction of the evolving starburst population in the local universe is assumed to be $\sim 10\%$ of the total, consistent with the local observed fraction of interacting galaxies. Franceschini et al. (2001) have fitted the IRAS $12 \mu\text{m}$ local galaxy luminosity function (LLF) with an analytic form and a given normalization, by sum-

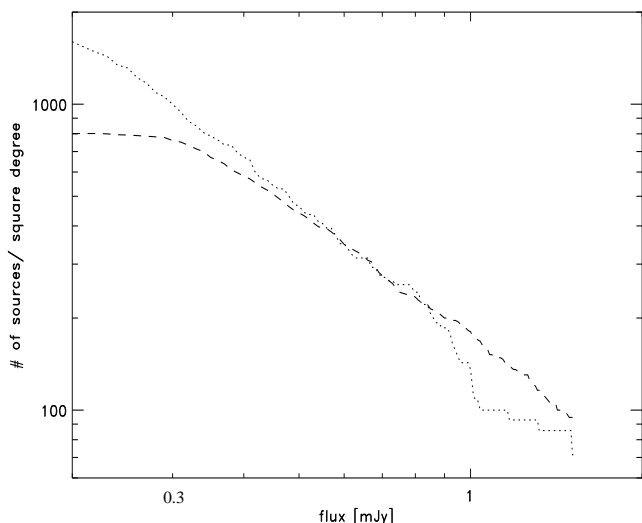


Fig. 15. Integral source counts for extragalactic ISOCAM sources detected at $14.3 \mu\text{m}$ in the Deep and Shallow survey, without areal and completeness correction. The dotted line refers to the Deep sample, the dashed line to the Shallow one.

ming the contribution of the three different basic populations (see discussion and details in their paper). In the new configuration, the luminosity and density evolution rate are kept unchanged, while the luminosity function of the evolving population has been slightly renormalized downward to better fit the SWIRE/Spitzer $24 \mu\text{m}$ counts (Franceschini et al. 2004, in prep). The two solutions are plotted in Figure 16: the dotted line traces the old predictions by Franceschini et al. (2001), the new ones are marked as a solid line. For comparison we report the recent evolution model by Pozzi et al. (2004, dot-dashed line), which is built to reproduce the brighter ELAIS counts (Gruppioni et al. 2002). The approach is similar to that presented by Franceschini et al. (2001), however Pozzi et al. (2004) start from a direct determination of the $15 \mu\text{m}$ LLF from the ELAIS southern field. Even if a better computation of the incompleteness of our catalogues is needed to constrain the faint end of the distribution, our results fully support the claims by previous works (Elbaz et al. 1999, Franceschini et al. 2001, Gruppioni et al. 2002) for the existence of an evolving population of infrared galaxies. Indeed, our data confirm the evident departure from non evolutionary model predictions: the dashed line in Figure 16 represents the expectations from a no-evolution model normalized to the IRAS $12 \mu\text{m}$ local luminosity function (Fang et al. 1998).

10. Summary and conclusions

The reduction technique of Lari et al. (2001) has been applied to the ISOCAM $14.3 \mu\text{m}$ observation of a region of 0.11 square arcminutes in the direction of the Lockman Hole. We produced a catalogue with 283 sources detected

above the $5\text{-}\sigma$ threshold with fluxes in the interval 0.1-8 mJy. This survey is intermediate between the ultra-deep surveys (like the HDF-North) and the shallow surveys in the ELAIS fields (Rowan-Robinson et al. 2003). The catalogue is 90% complete at 1 mJy. The positional accuracy, estimated from the cross-correlation of infrared and optical sources, is around 1.5 arcsec.

We have checked the calibration (essentially based on the cookbook factor, Blommaert et al. 2000) comparing the $14.3 \mu\text{m}$ measured fluxes with model predictions, and found a discrepancy of $\sim 10\%$ between the ISO and the IRAS zero points. We have taken into account this factor when computing galaxy counts, in order to compare different samples on the same flux scale (as done by Gruppioni et al. 2002 in the shallower ELAIS fields).

We found that the $6.7 \mu\text{m}/14.3 \mu\text{m}$ colour works well as a star/galaxy indicator: we have combined this method with the visual inspection of an optical image to classify all the catalogue sources and reject stars when computing galaxy counts.

The optical counterparts of the sources in the survey have been found by looking at the infrared contours overlaid on the optical image, making use of the radio detections when available, and computing the maximum likelihood for every possible optical association. For infrared extended and/or blended objects, we reported the list of possible optical associations. Only 15% of the $14.3 \mu\text{m}$ sources turned out to be optically empty fields (no reliable associations within a search radius of 10 arcseconds).

We discussed the $14.3 \mu\text{m}$ counts of extra-galactic sources. We obtained the number densities from the sample presented in this paper (Lockman Deep) and from the sample introduced in Paper I (Lockman Shallow). The two surveys are fully consistent, and these results support previous findings for a strong evolution of the infrared population. However a more detailed discussion will be presented in a forthcoming paper, given that the completeness of our sample drops at around ~ 0.5 mJy and extensive simulations are needed to recover the quantity of undetected sources as a function of the flux level.

Forthcoming papers will also present the spectroscopic follow-up observations made with the CFHT and Keck telescopes, the multi-wavelength spectral energy distributions and a cross-correlation between the infrared and radio sources in the field.

Finally, the recently launched Spitzer Space Telescope (25th of August 2003, Fazio et al., 1999) is not set to observe in the $14.3 \mu\text{m}$ channel in imaging mode (the closest ones are centred at 8 and $24 \mu\text{m}$). Only the IRS spectrograph can observe in this wavelength range, but it is not supposed to be used for surveys. This makes our set of data unique. However the planned observations of the Lockman Hole with Spitzer in its Guaranteed Time and in the SWIRE Legacy program (Lonsdale et al., 2003) will allow a more complete description of the SEDs of the objects detected by ISO, and will also extend the redshift flux density coverage.

Acknowledgements. We thank F. Pozzi for providing her source counts model in electronic form and C. Gruppioni for the reliabilities of the optical identifications. We are in debt to the referee, Carol J. Lonsdale, for helpful comments that improved the quality of the paper. G.R. wants to thank J. Manners for a careful reading of the paper. This work was partly supported by the "POE" EC TMR Network Programme (HPRN-AT-2000-00138).

References

- Altieri B., Metcalfe L., Kneib J. P., 1999, *A&A*, 343, L65
 Aussel, H., Alexander, D. M., 2001, *A&AS*, 198, 4910
 Beichman, C. A., Cutri, R., Jarrett, T., Stiening, R., Skrutskie, M., 2003 *AJ*, 125, 2521
 Bernstein, R., Freedman, W.L., Madore, B., 2002, *ApJ*, 571, 56
 Bertin, E., Arnouts, S., 1996, *A&AS*, 117, 393
 Bertin, E., Dennefeld, M., Moshir, M., 1997, *A&A*, 323, 685
 Blommaert, J., Metcalfe, L., Altieri B. et al., 2000, *Exp. Astr.*, 10, 241.
 Cesarsky, C. J., Abergel, A., Agnese, P. et al., 1996, *A&A*, 315, p.L32-L37
 Chary, R., Elbaz, D., 2001, *ApJ*, 556, 562
 Ciliegi, P., Zamorani, G., Hasinger, G. et al., 2003, *A&A*, 398, 901
 De Ruiter, H. R., Zamorani, G., Parma, P. et al., 1997, *A&A*, 319, 7
 Dole, H., Gispert, R., Lagache, G. et al., 2001, *A&A*, 372, 364
 Efstathiou, A., Oliver, S., Rowan-Robinson, M. et al., 2000, *MNRAS*, 319, 1169
 Elbaz, D., Cesarsky, C. J., Fadda, D. et al., 1999, *A&A* 351, L37
 Elbaz, D., Cesarsky, C. J., Chanical, P., et al. 2002, *A&A*, 384, 848
 Elbaz, D. & Cesarsky, C. J., 2003, *Science*, 300, 270
 Elbaz, D., Marcellac, D., Moy, E., 2004, astro-ph/0403209
 Fadda, D., Flores, H., Hasinger, G., et al. 2002, *A&A*, 383, 838
 Fadda, D., et al., 2004, *A&A* submitted (Paper I)
 Fang F., Shupe D., Xu C., Hacking P., 1998, *ApJ*, 500, 693
 Flores, H., Hammer, F., Thuan, T. X. et al. 1999, *ApJ*, 517, 148
 Franceschini, A., Danese, L., De Zotti, G., Xu, C., 1988, *MNRAS*, 233, 175
 Franceschini, A., Aussel, H., Cesarsky, C. J., Elbaz, D., Fadda, D., 2001, *A&A*, 378, 1
 Franceschini, A., Berta, S., Rigopoulou, D. et al., 2003, *A&A*, 403, 501
 Gonzalez-Solares, E.A., Perez-Fournon, I., Rowan-Robinson, M. et al., 2004, astro-ph/0402406
 Gregorich, D. T., Neugebauer, G., Soifer, B. T., Gunn, J. E., Herter, T. L., 1995, *AJ*, 110, p.259
 Gruppioni C., Lari C., Pozzi F. et al. 2002, *MNRAS*, 335, 831
 Hacking P., Houck J. R., Condon J. J., 1987, *ApJ*, 316, L15
 Hauser M. G. & Dwek E., 2001, *ARA&A*, 39, 249
 Hog, E., Fabricius, C., Makarov, V. V. et al. 2000, *A&A*, 357, 367
 Kawara, K., Matsuhara, H., Okuda, H. et al., 2004, *A&A*, 413, 843
 Kessler, M. F., Steinz, J. A., Anderegg, M. E. et al., 1996, *A&A*, 315, L27
 Lagache, G., Abergel, A., Boulanger, F., Desert, F. X., Puget, J.-L., 1999, *A&A*, 344, 322
 Lari, C., Pozzi, F., Gruppioni, C. et al., 2001, *MNRAS*, 325, 1173
 Lejeune, T., Cuisinier, F., Buser, R. 1998, *A&AS*, 130, 65
 Lockman, F. J., Jahoda, K., McCammon, D., 1986, *ApJ*, 302, 432
 Lonsdale C. J., Hacking P. B., Conrow T. P., Rowan-Robinson M., 1990, *ApJ*, 358, 60
 Lonsdale, C. J., Smith, Harding, E., Rowan-Robinson, M. et al. 2003, *PASP*, 115, 897
 Metcalfe, N., Shanks, T., Campos, A., McCracken, H. J., Fong, R., 2001, *MNRAS*, 323, 795
 Omont, A., Alard, C., Blommaert, J. A. D. L. et al., 1999, *A&A*, 348, 755
 Ott S., Gastaud R., Ali B. et al. 2001, in *Astronomical Data Analysis Software and Systems X*, ASP Conference Proceedings, Vol. 238.
 Pozzi, F., Ciliegi, P., Gruppioni, C. et al., 2003, *MNRAS*, 343, 1348
 Pozzi, F., Gruppioni, C., Oliver, S. et al., 2004, *ApJ*, 609, 122
 Rodighiero, G., Lari, C., Franceschini, A., Gregnanin, A., Fadda, D. 2003, *MNRAS*, 343, 1155
 Rodighiero, G. & Franceschini, A., 2004, *A&A*, 419, 55
 Rowan-Robinson, M., Clegg, P. E., Beichman, C. A. et al., 1984, *ApJ*, 278, L7
 Rowan-Robinson M., 2001, *ApJ*, 549, 745
 Rowan-Robinson, M., Lari, C., Perez-Fournon, I. et al. 2004, *MNRAS*, 351, 1290
 Soifer, B. T., Neugebauer, G., Helou, G. et al., 1984, *ApJ*, 278, L71
 Starck, J.-L., Aussel, H., Elbaz, D., Fadda, D. & Cesarsky, C.J., 1999, *A&AS*, 138,365
 Sutherland, W., Saunders, W., 1992, *MNRAS*, 259, 413
 Vaccari, M., Lari, C., Angeretti, L. et al. 2004, astro-ph/0404315
 Werner, M., Roellig, T. L., Low, F. J. et al. 2004, *ApJL*, in press
 Xu, C. K., Lonsdale, C. J., Shupe, D. L. et al. 2003, *ApJ*, 587, 90

Table 2. LW3 source catalogue in the deep Lockman Hole: highly reliable detections.

Nr	ID	RA	DEC	S/N	LW3 Flux	1.4Ghz	S/G	REL	r'	$\Delta(IR - opt)$
		(J2000)	(J2000)		[mJy]	[mag]			[mag]	["]
1	ISO.LHDS_J105121+572415	10:51:21.942	+57:24:15.48	313	8.518± 0.93	—	1	0.99	10.75	0.84
2	ISO.LHDS_J105303+571205	10:53:03.768	+57:12:05.66	168	4.991± 0.54	0.22	0	0.99	19.34	0.78
3	ISO.LHDS_J105227+571354	10:52:27.580	+57:13:54.48	169	*4.677± 0.49	—	0	0.80	21.49	1.12
4	ISO.LHDS_J105201+571044	10:52:01.174	+57:10:44.29	78	4.658± 0.51	—	1	0.99	10.97	4.30
5	ISO.LHDS_J105153+571900	10:51:53.682	+57:19:00.07	137	4.269± 0.46	—	1	0.99	10.66	2.57
6	ISO.LHDS_J105228+570918	10:52:28.591	+57:09:18.44	62	*3.940± 0.35	—	0	0.98	19.79	1.40
7	ISO.LHDS_J105143+572937	10:51:43.701	+57:29:37.57	75	*3.520± 0.32	0.21	0	0.99	16.39	0.78
8	ISO.LHDS_J105242+571914	10:52:42.468	+57:19:14.45	95	3.155± 0.34	0.22	0	0.99	17.55	0.50
9	ISO.LHDS_J105318+572141	10:53:18.929	+57:21:41.92	86	*3.093± 0.30	0.21	0	0.99	17.21	1.25
10	ISO.LHDS_J105242+572444	10:52:42.406	+57:24:44.72	102	3.032± 0.33	0.22	0	0.99	17.14	0.28
11	ISO.LHDS_J105231+571751	10:52:31.606	+57:17:51.90	75	2.807± 0.31	—	0	0.96	22.99	0.61
12	ISO.LHDS_J105113+571427	10:51:13.442	+57:14:27.78	83	2.379± 0.26	0.19	0	0.98	20.10	1.43
13	ISO.LHDS_J105252+572901	10:52:52.724	+57:29:01.01	76	2.193± 0.24	0.23	0	0.99	17.32	1.28
14	ISO.LHDS_J105217+572127	10:52:17.726	+57:21:27.63	43	1.373± 0.15	0.26	0	0.98	21.79	0.94
15	ISO.LHDS_J105200+571805	10:52:00.299	+57:18:05.87	48	1.367± 0.15	—	0	0.70	24.01	0.48
16	ISO.LHDS_J105310+571357	10:53:10.819	+57:13:57.10	43	1.354± 0.15	—	1	0.99	11.62	6.66
17	ISO.LHDS_J105307+571826	10:53:07.824	+57:18:26.78	42	1.346± 0.15	—	1	0.99	11.66	2.87
18	ISO.LHDS_J105058+572512	10:50:58.188	+57:25:12.67	42	1.296± 0.14	—	1	0.99	15.56	0.77
19	ISO.LHDS_J105255+571952	10:52:55.360	+57:19:52.10	24	*1.241± 0.12	0.19	0	0.54	24.30	2.43
20	ISO.LHDS_J105258+570925	10:52:58.243	+57:09:25.45	26	1.199± 0.13	—	0	0.99	17.93	1.13
21	ISO.LHDS_J105256+570829	10:52:56.814	+57:08:29.41	13	*0.957± 0.09	0.21	0	0.98	16.88	3.61
22	ISO.LHDS_J105237+571432	10:52:37.666	+57:14:32.79	30	0.942± 0.10	—	0	0.84	21.17	1.08
23	ISO.LHDS_J105043+571730	10:50:43.187	+57:17:30.98	13	*0.942± 0.06	—	0	0.98	18.99	3.70
24	ISO.LHDS_J105258+570842	10:52:58.849	+57:08:42.50	14	0.928± 0.11	—	0	—	B.F.	—
25	ISO.LHDS_J105200+571312	10:52:00.010	+57:13:12.12	24	0.921± 0.10	—	1	0.99	12.14	1.93
26	ISO.LHDS_J105257+571515	10:52:57.655	+57:15:15.80	33	0.917± 0.10	0.27	0	0.99	18.03	0.14
27	ISO.LHDS_J105218+572617	10:52:18.026	+57:26:17.21	30	0.916± 0.10	—	0	0.99	18.62	0.94
28	ISO.LHDS_J105135+572738	10:51:35.482	+57:27:38.80	26	0.914± 0.10	0.27	0	0.92	22.73	0.56
29	ISO.LHDS_J105227+571414	10:52:27.440	+57:14:14.69	24	*0.913± 0.09	—	0	0.99	19.85	0.63
30	ISO.LHDS_J105213+571605	10:52:13.475	+57:16:05.03	35	0.905± 0.10	0.22	0	0.96	22.52	0.69
31	ISO.LHDS_J105126+572200	10:51:26.558	+57:22:00.71	23	*0.880± 0.08	—	0	0.92	19.47	1.67
32	ISO.LHDS_J105135+572959	10:51:35.984	+57:29:59.86	31	0.871± 0.09	—	0	0.91	21.82	1.47
33	ISO.LHDS_J105239+572432	10:52:39.569	+57:24:32.09	25	0.858± 0.09	0.27	0	0.99	17.73	0.54
34	ISO.LHDS_J105306+572807	10:53:06.764	+57:28:07.49	23	*0.856± 0.06	—	0	0.97	22.02	1.08
35	ISO.LHDS_J105113+571723	10:51:13.297	+57:17:23.08	27	0.854± 0.09	—	0	—	B.F.	—
36	ISO.LHDS_J105234+572643	10:52:34.978	+57:26:43.88	25	0.847± 0.09	—	0	0.59	21.17	1.30
37	ISO.LHDS_J105255+572223	10:52:55.105	+57:22:23.69	27	0.833± 0.09	—	0	0.99	18.83	0.84
38	ISO.LHDS_J105056+571632	10:50:56.774	+57:16:32.39	29	*0.805± 0.08	0.24	0	0.71	20.49	1.72
39	ISO.LHDS_J105225+571130	10:52:25.642	+57:11:30.38	19	0.804± 0.09	0.26	0	0.99	17.73	1.30
40	ISO.LHDS_J105308+571322	10:53:08.251	+57:13:22.44	21	*0.795± 0.09	—	0	0.99	19.57	0.87
41	ISO.LHDS_J105142+571503	10:51:42.063	+57:15:03.95	23	*0.794± 0.08	0.26	0	0.90	18.58	2.18
42	ISO.LHDS_J105250+572608	10:52:50.254	+57:26:08.44	21	0.791± 0.09	—	1	0.99	11.83	5.24
43	ISO.LHDS_J105315+571939	10:53:15.736	+57:19:39.18	19	*0.768± 0.06	—	0	0.90	20.73	2.88
44	ISO.LHDS_J105307+571500	10:53:07.870	+57:15:00.84	18	0.767± 0.09	0.28	0	0.90	21.68	1.01
45	ISO.LHDS_J105235+572652	10:52:35.376	+57:26:52.60	26	0.767± 0.08	0.23	0	0.98	19.16	0.74
46	ISO.LHDS_J105059+571932	10:50:59.454	+57:19:32.29	23	0.743± 0.08	—	0	0.82	20.56	3.72
47	ISO.LHDS_J105259+573017	10:52:59.750	+57:30:17.30	18	0.741± 0.08	—	0	0.90	22.36	2.81
48	ISO.LHDS_J105142+572124	10:51:42.923	+57:21:24.50	17	*0.732± 0.06	—	0	0.99	18.65	2.10
49	ISO.LHDS_J105242+573138	10:52:42.959	+57:31:38.58	12	0.716± 0.09	—	0	0.99	17.07	0.96
50	ISO.LHDS_J105215+571319	10:52:15.328	+57:13:19.02	18	0.666± 0.07	—	0	0.92	21.38	0.96
51	ISO.LHDS_J105215+572634	10:52:15.140	+57:26:34.09	23	0.647± 0.07	—	0	0.98	19.31	1.41
52	ISO.LHDS_J105109+572525	10:51:09.478	+57:25:25.14	22	0.630± 0.07	—	0	0.99	21.09	1.03
53	ISO.LHDS_J105053+572425	10:50:53.410	+57:24:25.78	15	0.627± 0.07	0.23	0	0.99	19.05	0.26
54	ISO.LHDS_J105110+572143	10:51:10.919	+57:21:43.18	16	*0.616± 0.06	—	1	0.99	19.35	2.23
55	ISO.LHDS_J105305+572331	10:53:05.289	+57:23:31.37	23	0.604± 0.06	—	0	0.97	21.67	0.97
56	ISO.LHDS_J105058+573354	10:50:58.401	+57:33:54.59	15	0.604± 0.07	—	0	0.89	23.17	2.04
57	ISO.LHDS_J105233+570933	10:52:33.252	+57:09:33.92	9	*0.580± 0.07	—	0	0.99	19.25	2.07
58	ISO.LHDS_J105314+573021	10:53:14.378	+57:30:21.49	13	0.557± 0.06	0.22	0	0.84	23.71	2.10
59	ISO.LHDS_J105121+571939	10:51:21.361	+57:19:39.07	20	0.547± 0.06	—	0	0.71	23.62	1.79
60	ISO.LHDS_J105113+572655	10:51:13.383	+57:26:55.25	16	0.547± 0.06	0.25	0	0.84	23.11	1.35
61	ISO.LHDS_J105206+571524	10:52:06.316	+57:15:24.51	18	0.537± 0.06	—	0	0.99	18.47	0.78
62	ISO.LHDS_J105215+572942	10:52:15.711	+57:29:42.65	19	0.529± 0.06	—	0	0.96	22.63	0.53
63	ISO.LHDS_J105203+572707	10:52:03.629	+57:27:07.90	17	0.525± 0.06	—	0	0.78	24.22	0.89
64	ISO.LHDS_J105321+572726	10:53:21.295	+57:27:26.24	15	0.523± 0.06	—	0	0.92	22.38	3.15
65	ISO.LHDS_J105300+571341	10:53:00.581	+57:13:41.45	17	0.512± 0.06	—	1	0.99	18.63	2.93
66	ISO.LHDS_J105205+572522	10:52:05.040	+57:25:22.54	18	0.508± 0.06	—	0	0.99	19.13	1.44
67	ISO.LHDS_J105218+571024	10:52:18.301	+57:10:24.17	11	*0.505± 0.04	—	0	0.98	21.48	2.16
68	ISO.LHDS_J105245+571424	10:52:45.868	+57:14:24.61	13	0.502± 0.06	—	0	0.99	21.15	0.44
69	ISO.LHDS_J105207+571500	10:52:07.250	+57:15:00.18	16	0.499± 0.05	—	1	0.99	16.29	1.36
70	ISO.LHDS_J105148+573248	10:51:48.860	+57:32:48.16	11	0.497± 0.06	0.19	0	0.95	22.26	1.28
71	ISO.LHDS_J105225+571339	10:52:25.738	+57:13:39.61	16	0.490± 0.05	—	0	0.99	21.26	1.56
72	ISO.LHDS_J105301+571456	10:53:01.153	+57:14:56.64	14	0.486± 0.05	—	0	0.94	20.93	1.26
73	ISO.LHDS_J105117+571426	10:51:17.842	+57:14:26.13	16	*0.485± 0.05	—	0	0.91	22.05	1.28
74	ISO.LHDS_J105237+572148	10:52:37.549	+57:21:48.46	17	*0.472± 0.05	—	0	0.99	21.01	1.45
75	ISO.LHDS_J105051+572922	10:50:51.113	+57:29:22.96	13	0.470± 0.05	—	0	0.98	20.04	1.31
76	ISO.LHDS_J105251+572736	10:52:51.846	+57:27:36.93	15	0.468± 0.05	—	1	0.99	12.26	1.70
77	ISO.LHDS_J105047+571856	10:50:47.763	+57:18:56.10	12	0.463± 0.05	—	0	0.88	22.74	1.62
78	ISO.LHDS_J105125+572543	10:51:25.227	+57:25:43.70	15	0.458± 0.05	—	0	0.94	21.92	1.97
79	ISO.LHDS_J105058+572544	10:50:58.844	+57:25:44.55	14	0.458± 0.05	—	0	0.98	19.58	0.87
80	ISO.LHDS_J105155+571301	10:51:55.113	+57:13:01.90	19	0.451± 0.05	—	0	0.97	21.29	1.19
81	ISO.LHDS_J105233+571233	10:52:33.447	+57:12:33.89	13	0.446± 0.05	—	1	0.99	16.74	1.09
82	ISO.LHDS_J105228+571146	10:52:28.161	+57:11:46.84	12	0.445± 0.05	—	0	0.99	18.37	1.72
83	ISO.LHDS_J105253+572419	10:52:53.804	+57:24:19.28	15	0.437± 0.05	—	0	0.98	21.65	1.64
84	ISO.LHDS_J105059+572427	10:50:59.000	+57:24:27.00	11	*0.435± 0.05	—	1	0.99	15.93	2.11
85	ISO.LHDS_J105151+572448	10:51:51.930	+57:24:48.59	14	0.433± 0.05	—	0	0.99	21.07	1.53
86	ISO.LHDS_J105112+571334	10:51:12.590	+57:13:34.31	9	0.432± 0.05	—	0	0.99	20.40	1.18
87	ISO.LHDS_J105055+571219	10:50:55.894	+57:12:19.64	9	0.430± 0.06	—	0	—	B.F.	—
88	ISO.LHDS_J105200+572409	10:52:00.170	+57:24:09.97	16	0.429± 0.05	—	0	0.93	21.59	2.64
89	ISO.LHDS_J105212+572453	10:52:12.577	+57:24:53.24	16	0.414± 0.05	0.23	0	0.99	20.99	0.61
90	ISO.LHDS_J105103+572039	10:51:03.580	+57:20:39.57	20	0.411± 0.04	—	0	0.99	19.63	2.53
91	ISO.LHDS_J105240+571601	10:52:40.248	+57:16:01.36	9	0.403± 0.05	—	0	0.96	22.42	1.77
92	ISO.LHDS_J105151+571332	10:51:51.303	+57:13:32.56	14	0.401± 0.					

Nr	ID	RA (J2000)	DEC (J2000)	S/N	LW3 Flux [mJy]	1.4Ghz [mJy]	S/G	REL	r' [mag]	$\Delta(IR - opt)$ [']
101	ISO.LHDS_J105129+571606	10:51:29.824	+57:16:06.38	10	0.378± 0.05	—	0	0.68	22.88	0.61
102	ISO.LHDS_J105258+572749	10:52:58.276	+57:27:49.79	9	0.378± 0.05	—	0	0.99	19.39	1.06
103	ISO.LHDS_J105154+572408	10:51:54.323	+57:24:08.67	11	0.375± 0.04	—	0	0.92	22.09	2.72
104	ISO.LHDS_J105104+573311	10:51:04.303	+57:33:11.26	5	0.375± 0.06	—	0	0.77	21.31	1.85
105	ISO.LHDS_J105235+570903	10:52:35.647	+57:09:03.47	6	0.373± 0.06	—	0	—	B.F.	—
106	ISO.LHDS_J105106+573336	10:51:06.829	+57:33:36.75	10	0.373± 0.05	—	0	—	B.F.	—
107	ISO.LHDS_J105243+571253	10:52:43.040	+57:12:53.66	8	*0.367± 0.03	—	0	0.97	21.47	1.63
108	ISO.LHDS_J105232+572450	10:52:32.019	+57:24:50.20	14	0.367± 0.04	—	0	0.98	21.74	1.37
109	ISO.LHDS_J105255+571149	10:52:55.723	+57:11:49.60	10	0.357± 0.04	—	0	0.96	21.40	0.75
110	ISO.LHDS_J105324+572823	10:53:24.802	+57:28:23.09	12	0.357± 0.04	—	0	0.97	20.61	0.37
111	ISO.LHDS_J105149+573303	10:51:49.991	+57:33:03.80	7	0.355± 0.05	—	1	0.58	19.63	4.59
112	ISO.LHDS_J105100+571519	10:51:00.123	+57:15:19.37	10	0.354± 0.04	—	0	—	B.F.	—
113	ISO.LHDS_J105203+572518	10:52:03.339	+57:25:18.80	14	0.352± 0.04	—	0	0.71	18.59	3.25
114	ISO.LHDS_J105128+572854	10:51:28.991	+57:28:54.17	11	0.352± 0.04	—	0	0.99	20.74	0.51
115	ISO.LHDS_J105313+572845	10:53:13.044	+57:28:45.12	14	0.352± 0.04	—	0	0.99	19.11	0.39
116	ISO.LHDS_J105112+571214	10:51:12.518	+57:12:14.97	10	0.351± 0.04	—	0	0.68	21.86	2.56
117	ISO.LHDS_J105136+572515	10:51:36.070	+57:25:15.37	10	0.348± 0.04	—	0	0.93	23.50	0.49
118	ISO.LHDS_J105154+571330	10:51:54.132	+57:13:30.25	10	*0.345± 0.03	—	0	—	B.F.	—
119	ISO.LHDS_J105315+571826	10:53:15.048	+57:18:26.31	11	0.336± 0.04	—	0	0.99	21.08	1.87
120	ISO.LHDS_J105104+572737	10:51:04.259	+57:27:37.69	10	0.332± 0.04	—	0	0.99	20.49	1.77
121	ISO.LHDS_J105309+571700	10:53:09.110	+57:17:00.65	8	0.330± 0.04	—	0	0.95	15.63	3.40
122	ISO.LHDS_J105057+572603	10:50:57.371	+57:26:03.37	8	0.330± 0.04	—	1	0.99	15.89	1.66
123	ISO.LHDS_J105301+571539	10:53:01.868	+57:15:39.80	12	0.330± 0.04	—	0	0.90	21.95	2.58
124	ISO.LHDS_J105111+573311	10:51:11.679	+57:33:11.18	7	0.325± 0.05	—	0	0.98	18.97	3.96
125	ISO.LHDS_J105201+572920	10:52:01.924	+57:29:20.31	9	0.323± 0.04	—	1	0.99	16.17	2.07
126	ISO.LHDS_J105232+572158	10:52:32.387	+57:21:58.22	8	0.322± 0.04	—	0	0.98	21.06	1.22
127	ISO.LHDS_J105141+571150	10:51:41.256	+57:11:50.81	8	0.320± 0.04	—	0	0.99	21.03	1.21
128	ISO.LHDS_J105112+573118	10:51:12.755	+57:31:18.77	11	0.318± 0.04	—	0	0.98	21.52	1.23
129	ISO.LHDS_J105220+573132	10:52:20.959	+57:31:32.42	7	0.317± 0.04	—	0	0.63	22.78	1.13
130	ISO.LHDS_J105049+572901	10:50:49.965	+57:29:01.07	7	0.311± 0.04	—	0	0.00	25.06	7.62
131	ISO.LHDS_J105051+571515	10:50:51.243	+57:15:15.64	10	0.306± 0.04	—	0	0.99	20.72	1.87
132	ISO.LHDS_J105056+573218	10:50:56.706	+57:32:18.16	6	0.305± 0.04	—	0	0.89	23.09	2.09
133	ISO.LHDS_J105123+571228	10:51:23.486	+57:12:28.15	8	0.305± 0.04	—	0	—	B.F.	—
134	ISO.LHDS_J105300+571651	10:53:00.781	+57:16:51.31	9	0.304± 0.04	—	0	0.99	19.24	0.67
135	ISO.LHDS_J105054+572843	10:50:54.099	+57:28:43.72	9	0.303± 0.04	—	0	0.77	24.17	1.22
136	ISO.LHDS_J105119+571954	10:51:19.219	+57:19:54.88	10	0.302± 0.03	—	0	—	B.F.	—
137	ISO.LHDS_J105218+571020	10:52:18.649	+57:10:20.62	8	*0.297± 0.02	—	0	—	B.F.	—
138	ISO.LHDS_J105253+571602	10:52:53.039	+57:16:02.33	11	0.297± 0.03	—	0	0.99	20.62	0.96
139	ISO.LHDS_J105204+573030	10:52:04.502	+57:30:30.18	10	0.296± 0.03	—	0	0.87	22.17	2.60
140	ISO.LHDS_J105120+573238	10:51:20.285	+57:32:38.41	8	0.295± 0.04	—	0	0.26	25.25	1.83
141	ISO.LHDS_J105231+571549	10:52:31.435	+57:15:49.93	9	0.294± 0.03	—	1	0.99	18.63	3.92
142	ISO.LHDS_J105143+571836	10:51:43.377	+57:18:36.16	10	0.294± 0.03	—	0	0.96	22.84	0.93
143	ISO.LHDS_J105235+572330	10:52:35.173	+57:23:30.25	8	0.289± 0.04	—	0	0.99	19.95	0.81
144	ISO.LHDS_J105059+572715	10:50:59.864	+57:27:15.85	8	0.287± 0.04	—	0	0.87	22.92	1.32
145	ISO.LHDS_J105148+571631	10:51:48.243	+57:16:31.69	8	0.286± 0.04	—	0	0.90	19.76	2.70
146	ISO.LHDS_J105042+571705	10:50:42.627	+57:17:05.05	8	0.285± 0.04	—	0	—	B.F.	—
147	ISO.LHDS_J105139+573108	10:51:39.363	+57:31:08.45	9	0.285± 0.03	—	0	0.95	22.57	1.45
148	ISO.LHDS_J105314+571933	10:53:14.232	+57:19:33.71	6	0.285± 0.04	—	0	0.72	25.00	1.63
149	ISO.LHDS_J105310+572324	10:53:10.719	+57:23:24.65	9	0.284± 0.03	—	0	0.96	20.64	3.73
150	ISO.LHDS_J105231+573204	10:52:31.176	+57:32:04.74	5	0.283± 0.05	—	0	0.99	22.75	0.64
151	ISO.LHDS_J105247+572117	10:52:47.938	+57:21:17.67	6	0.283± 0.04	—	0	0.99	20.01	1.23
152	ISO.LHDS_J105044+571539	10:50:44.609	+57:15:39.66	7	0.282± 0.04	—	0	—	B.F.	—
153	ISO.LHDS_J105242+572846	10:52:42.144	+57:28:46.06	7	0.281± 0.04	—	0	0.67	15.63	5.44
154	ISO.LHDS_J105219+571528	10:52:19.309	+57:15:28.09	7	0.280± 0.04	—	0	0.94	22.00	0.93
155	ISO.LHDS_J105311+571238	10:53:11.205	+57:12:38.29	8	0.279± 0.04	—	0	0.63	23.11	3.04
156	ISO.LHDS_J105159+572542	10:51:59.209	+57:25:42.45	8	0.278± 0.04	—	0	0.93	21.82	3.68
157	ISO.LHDS_J105219+572922	10:52:19.548	+57:29:22.13	10	0.278± 0.03	—	0	0.95	21.70	2.47
158	ISO.LHDS_J105115+571150	10:51:15.499	+57:11:50.91	6	0.278± 0.04	—	0	0.78	22.79	3.21
159	ISO.LHDS_J105151+572806	10:51:51.333	+57:28:06.46	8	0.273± 0.03	—	0	0.65	22.66	2.09
160	ISO.LHDS_J105100+571955	10:51:00.971	+57:19:55.27	8	0.273± 0.03	—	0	0.61	21.89	2.13
161	ISO.LHDS_J105106+571429	10:51:06.149	+57:14:29.43	8	0.271± 0.03	—	0	0.91	22.48	1.39
162	ISO.LHDS_J105225+572246	10:52:25.062	+57:22:46.04	9	0.271± 0.03	0.29	0	0.99	21.50	1.53
163	ISO.LHDS_J105057+572821	10:50:57.516	+57:28:21.41	8	0.271± 0.03	—	0	0.77	22.36	4.49
164	ISO.LHDS_J105232+572837	10:52:32.520	+57:28:37.47	7	0.269± 0.03	—	0	0.62	23.46	3.61
165	ISO.LHDS_J105057+571333	10:50:57.441	+57:13:33.28	7	*0.268± 0.03	—	0	0.97	19.78	3.79
166	ISO.LHDS_J105048+572520	10:50:48.092	+57:25:20.68	8	0.267± 0.04	—	0	0.99	19.77	1.15
167	ISO.LHDS_J105108+572711	10:51:08.091	+57:27:11.26	10	0.266± 0.03	—	0	0.97	22.26	0.27
168	ISO.LHDS_J105257+571154	10:52:57.416	+57:11:54.47	7	0.263± 0.03	—	0	0.96	22.93	0.81
169	ISO.LHDS_J105237+571342	10:52:37.978	+57:13:42.31	8	0.260± 0.03	—	0	0.11	24.87	4.62
170	ISO.LHDS_J105144+571720	10:51:44.428	+57:17:20.51	8	0.258± 0.03	0.27	0	0.94	22.07	1.05
171	ISO.LHDS_J105236+573104	10:52:36.111	+57:31:04.19	5	0.257± 0.04	—	0	0.98	21.04	1.42
172	ISO.LHDS_J105226+573130	10:52:26.002	+57:31:30.96	6	0.255± 0.04	—	0	0.70	22.66	3.87
173	ISO.LHDS_J105219+571854	10:52:19.678	+57:18:54.14	8	0.253± 0.03	—	0	0.97	20.44	1.90
174	ISO.LHDS_J105141+571953	10:51:41.196	+57:19:53.12	9	0.250± 0.03	0.22	0	0.85	22.01	2.25
175	ISO.LHDS_J105218+572150	10:52:18.898	+57:21:50.09	7	0.250± 0.03	—	0	0.95	18.31	2.73
176	ISO.LHDS_J105124+571523	10:51:24.341	+57:15:23.87	8	0.250± 0.03	—	0	0.97	20.60	3.42
177	ISO.LHDS_J105108+573343	10:51:08.231	+57:33:43.40	6	0.250± 0.04	—	0	0.89	23.17	2.04
178	ISO.LHDS_J105213+571138	10:52:13.742	+57:11:38.72	7	0.249± 0.03	—	0	0.51	22.37	3.20
179	ISO.LHDS_J105130+572304	10:51:30.287	+57:23:04.71	6	0.249± 0.04	—	0	—	B.F.	—
180	ISO.LHDS_J105125+572901	10:51:25.158	+57:29:01.69	5	0.248± 0.04	—	1	0.98	21.76	0.14
181	ISO.LHDS_J105118+571500	10:51:18.171	+57:15:00.87	7	0.247± 0.03	—	0	—	B.F.	—
182	ISO.LHDS_J105119+571424	10:51:19.649	+57:14:24.12	7	0.246± 0.03	—	0	0.73	23.76	1.43
183	ISO.LHDS_J105317+571620	10:53:17.192	+57:16:20.06	8	0.246± 0.03	—	0	—	B.F.	—
184	ISO.LHDS_J105227+573125	10:52:27.095	+57:31:25.52	7	0.244± 0.03	—	0	—	B.F.	—
185	ISO.LHDS_J105129+571644	10:51:29.792	+57:16:44.01	7	0.243± 0.03	—	0	—	B.F.	—
186	ISO.LHDS_J105227+571557	10:52:27.426	+57:15:57.50	7	0.242± 0.03	—	0	0.56	23.91	1.74
187	ISO.LHDS_J105251+571540	10:52:51.528	+57:15:40.16	7	0.242± 0.03	—	0	0.53	23.36	2.90
188	ISO.LHDS_J105319+571850	10:53:19.229	+57:18:50.11	6	0.242± 0.03	0.20	0	0.99	19.05	2.58
189	ISO.LHDS_J105228+571152	10:52:28.369	+57:11:52.85	12	*0.242± 0.01	—	0	0.93	18.37	4.66
190	ISO.LHDS_J105055+571608	10:50:55.811	+57:16:08.53	8	0.239± 0.03	—	0	0.98	20.65	1.72
191	ISO.LHDS_J105209+573022	10:52:09.222	+57:30:22.13	9	0.239± 0.03	—	0	0.90	21.00	2.73
192	ISO.LHDS_J105307+572841	10:53:07.022	+57:28:41.38	7	0.235± 0.03	—	0	0.99	18.50	2.10
193	ISO.LHDS_J105110+571603	10:51:10.634	+57:16:03.92	8	0.235± 0.03	0.30	0	0.99	20.78	2.01
194	ISO.LHDS_J105226+572330	10:52:26.5								

Table 3. LW3 source catalogue in the deep Lockman Hole: faint detections.

Nr	ID	RA (J2000)	DEC (J2000)	S/N	LW3 Flux [mJy]	1.4Ghz [mJy]	S/G	REL	r' [mag]	$\Delta(IR - opt)$ [$^{\circ}$]
207	ISO.LHDS_J105147+572214	10:51:47.452	+57:22:14.47	6	0.218± 0.03	—	0	0.85	23.67	1.70
208	ISO.LHDS_J105145+572821	10:51:45.117	+57:28:21.20	7	0.217± 0.03	—	0	0.56	23.09	3.60
209	ISO.LHDS_J105242+571346	10:52:42.653	+57:13:46.36	6	0.215± 0.03	—	0	0.76	24.18	0.63
210	ISO.LHDS_J105208+572556	10:52:08.249	+57:25:56.04	9	0.215± 0.03	—	0	0.96	22.81	0.56
211	ISO.LHDS_J105258+571308	10:52:58.413	+57:13:08.81	7	0.214± 0.03	—	0	—	B.F.	—
212	ISO.LHDS_J105258+571712	10:52:58.481	+57:17:12.47	7	0.214± 0.03	—	0	0.50	23.35	4.40
213	ISO.LHDS_J105238+572335	10:52:38.760	+57:23:35.88	8	0.213± 0.03	—	0	0.61	23.48	1.38
214	ISO.LHDS_J105241+571311	10:52:41.380	+57:13:11.67	5	0.212± 0.03	—	0	0.52	24.41	2.88
215	ISO.LHDS_J105133+571500	10:51:33.352	+57:15:00.27	7	0.212± 0.03	—	0	0.96	22.91	0.52
216	ISO.LHDS_J105209+572527	10:52:09.157	+57:25:27.52	9	0.211± 0.02	—	0	—	B.F.	—
217	ISO.LHDS_J105313+571238	10:53:13.021	+57:12:38.82	6	0.211± 0.03	—	0	0.98	21.82	1.27
218	ISO.LHDS_J105136+571615	10:51:36.660	+57:16:15.82	8	0.210± 0.03	—	0	0.98	21.64	0.95
219	ISO.LHDS_J105248+571205	10:52:48.276	+57:12:05.15	6	0.210± 0.03	—	0	0.98	21.51	0.72
220	ISO.LHDS_J105258+571647	10:52:58.635	+57:16:47.57	6	0.205± 0.03	—	0	0.27	22.36	6.16
221	ISO.LHDS_J105325+572909	10:53:25.217	+57:29:09.08	7	0.205± 0.03	0.20	0	0.99	17.67	1.92
222	ISO.LHDS_J105148+571917	10:51:48.081	+57:19:17.37	6	0.204± 0.03	—	0	0.96	20.76	2.35
223	ISO.LHDS_J105300+572028	10:53:00.179	+57:20:28.66	5	0.204± 0.03	—	0	0.89	22.70	3.04
224	ISO.LHDS_J105134+572919	10:51:34.445	+57:29:19.66	6	0.201± 0.03	—	0	0.71	23.66	1.62
225	ISO.LHDS_J105058+571827	10:50:58.041	+57:18:27.51	6	0.200± 0.03	—	0	0.99	20.35	1.13
226	ISO.LHDS_J105100+572430	10:51:00.426	+57:24:30.51	5	0.199± 0.03	—	0	0.99	19.60	2.19
227	ISO.LHDS_J105159+571953	10:51:59.513	+57:19:53.77	7	0.197± 0.03	—	0	—	B.F.	—
228	ISO.LHDS_J105059+572209	10:50:59.928	+57:22:09.13	6	0.196± 0.03	—	0	0.92	20.17	4.25
229	ISO.LHDS_J105128+572735	10:51:28.453	+57:27:35.04	8	0.195± 0.02	—	0	0.74	22.05	3.92
230	ISO.LHDS_J105058+572018	10:50:58.185	+57:20:18.88	6	0.195± 0.03	—	0	0.86	22.37	1.17
231	ISO.LHDS_J105141+571603	10:51:41.289	+57:16:03.62	8	0.194± 0.02	—	0	0.74	23.00	4.16
232	ISO.LHDS_J105108+571403	10:51:08.218	+57:14:03.73	6	0.193± 0.03	—	0	—	B.F.	—
233	ISO.LHDS_J105314+572507	10:53:14.805	+57:25:07.55	6	0.192± 0.03	—	0	0.89	23.07	1.94
234	ISO.LHDS_J105312+571441	10:53:12.472	+57:14:41.83	5	0.191± 0.03	—	0	0.90	21.13	3.70
235	ISO.LHDS_J105112+572629	10:51:12.453	+57:26:29.73	7	0.190± 0.02	—	0	0.76	22.06	4.03
236	ISO.LHDS_J105202+571536	10:52:02.000	+57:15:36.90	6	0.190± 0.03	—	0	0.53	22.82	4.20
237	ISO.LHDS_J105245+572323	10:52:45.596	+57:23:23.12	5	0.190± 0.03	—	0	0.99	18.84	0.76
238	ISO.LHDS_J105145+572229	10:51:45.038	+57:22:29.88	5	0.190± 0.03	—	0	0.98	21.47	2.07
239	ISO.LHDS_J105144+572414	10:51:44.867	+57:24:14.00	5	0.189± 0.03	—	0	—	B.F.	—
240	ISO.LHDS_J105240+572143	10:52:40.781	+57:21:43.64	6	0.188± 0.03	—	0	—	B.F.	—
241	ISO.LHDS_J105215+571349	10:52:15.232	+57:13:49.97	6	*0.186± 0.02	—	1	0.99	16.43	3.92
242	ISO.LHDS_J105103+571501	10:51:03.043	+57:15:01.62	6	0.185± 0.03	—	0	0.97	22.34	1.31
243	ISO.LHDS_J105203+572746	10:52:03.725	+57:27:46.97	6	0.184± 0.03	—	0	—	B.F.	—
244	ISO.LHDS_J105211+571637	10:52:11.074	+57:16:37.58	6	0.179± 0.02	—	0	0.93	21.75	2.97
245	ISO.LHDS_J105316+571937	10:53:16.852	+57:19:37.54	7	0.177± 0.02	—	0	0.58	24.00	1.67
246	ISO.LHDS_J105044+571806	10:50:44.456	+57:18:06.82	5	0.174± 0.03	—	0	0.86	22.82	2.42
247	ISO.LHDS_J105246+571747	10:52:46.136	+57:17:47.34	5	0.173± 0.03	—	0	0.97	20.65	2.01
248	ISO.LHDS_J105054+571641	10:50:54.843	+57:16:41.72	6	0.172± 0.02	—	0	0.99	21.75	1.30
249	ISO.LHDS_J105231+572458	10:52:31.639	+57:24:58.77	6	0.172± 0.02	—	0	—	B.F.	—
250	ISO.LHDS_J105301+571711	10:53:01.910	+57:17:11.61	5	0.171± 0.03	—	0	0.82	22.73	2.68
251	ISO.LHDS_J105103+571419	10:51:03.867	+57:14:19.77	5	0.170± 0.03	—	0	0.93	22.46	2.50
252	ISO.LHDS_J105254+571456	10:52:54.063	+57:14:56.91	6	0.170± 0.02	—	0	0.99	19.87	1.90
253	ISO.LHDS_J105115+572528	10:51:15.654	+57:25:28.98	5	0.166± 0.03	—	0	0.66	24.15	0.71
254	ISO.LHDS_J105135+572550	10:51:35.535	+57:25:50.52	6	0.166± 0.02	—	0	0.90	21.34	4.32
255	ISO.LHDS_J105308+571721	10:53:08.845	+57:17:21.61	5	0.165± 0.02	—	0	0.98	20.85	0.94
256	ISO.LHDS_J105126+572453	10:51:26.447	+57:24:53.81	6	0.165± 0.02	—	0	—	B.F.	—
257	ISO.LHDS_J105242+572157	10:52:42.161	+57:21:57.83	5	0.163± 0.02	—	0	—	B.F.	—
258	ISO.LHDS_J105256+572743	10:52:56.150	+57:27:43.16	5	0.163± 0.02	—	0	0.98	21.09	2.33
259	ISO.LHDS_J105206+572301	10:52:06.176	+57:23:01.05	7	0.160± 0.02	—	0	0.99	20.71	1.09
260	ISO.LHDS_J105256+572345	10:52:56.086	+57:23:45.69	5	0.156± 0.02	—	0	—	B.F.	—
261	ISO.LHDS_J105043+571545	10:50:43.697	+57:15:45.37	5	0.154± 0.02	—	0	0.50	23.35	3.92
262	ISO.LHDS_J105149+571740	10:51:49.589	+57:17:40.46	5	0.154± 0.02	—	0	0.97	22.20	1.04
263	ISO.LHDS_J105155+572512	10:51:55.717	+57:25:12.20	5	0.154± 0.02	—	1	0.99	16.31	3.95
264	ISO.LHDS_J105219+571826	10:52:19.155	+57:18:26.54	5	0.153± 0.02	—	0	0.57	22.71	4.87
265	ISO.LHDS_J105213+571748	10:52:13.290	+57:17:48.79	6	0.151± 0.02	—	0	—	B.F.	—
266	ISO.LHDS_J105049+571511	10:50:49.500	+57:15:11.71	5	0.149± 0.02	—	0	0.96	22.08	2.09
267	ISO.LHDS_J105303+572330	10:53:03.037	+57:23:30.51	5	0.149± 0.02	—	0	—	B.F.	—
268	ISO.LHDS_J105115+571142	10:51:15.325	+57:11:42.84	6	0.148± 0.02	—	0	0.65	24.28	2.29
269	ISO.LHDS_J105112+572946	10:51:12.227	+57:29:46.32	5	0.148± 0.02	—	0	0.51	22.30	4.56
270	ISO.LHDS_J105256+571132	10:52:56.350	+57:11:32.05	5	0.147± 0.02	—	0	0.75	23.52	1.98
271	ISO.LHDS_J105214+572704	10:52:14.191	+57:27:04.86	5	0.145± 0.02	—	0	—	B.F.	—
272	ISO.LHDS_J105115+572501	10:51:15.906	+57:25:01.36	6	0.139± 0.02	—	0	0.98	21.95	0.84
273	ISO.LHDS_J105236+571844	10:52:36.396	+57:18:44.71	5	0.135± 0.02	—	0	0.98	21.64	1.28
274	ISO.LHDS_J105251+571120	10:52:51.086	+57:11:20.60	5	0.132± 0.02	—	0	—	B.F.	—
275	ISO.LHDS_J105101+572005	10:51:01.692	+57:20:05.20	5	0.132± 0.02	—	0	—	B.F.	—
276	ISO.LHDS_J105304+572322	10:53:04.482	+57:23:22.69	5	0.121± 0.02	—	0	0.63	24.99	0.75
277	ISO.LHDS_J105242+571251	10:52:42.361	+57:12:51.42	8	*0.118± 0.01	—	0	—	B.F.	—
278	ISO.LHDS_J105150+573240	10:51:50.650	+57:32:40.77	5	0.103± 0.01	—	0	0.60	18.69	4.99
279	ISO.LHDS_J105324+572903	10:53:24.881	+57:29:03.59	5	0.085± 0.01	—	0	0.87	23.33	2.14
280	ISO.LHDS_J105044+571725	10:50:44.228	+57:17:25.51	5	0.059± 0.01	—	0	—	B.F.	—
281	ISO.LHDS_J105209+572532	10:52:09.942	+57:25:32.29	5	0.058± 0.01	—	0	0.88	22.63	2.94
282	ISO.LHDS_J105043+571722	10:50:43.731	+57:17:22.28	5	0.055± 0.01	—	0	—	B.F.	3.12
283	ISO.LHDS_J105241+571917	10:52:41.206	+57:19:17.77	5	0.045± 0.01	—	0	0.80	22.56	3.15